Magma oscillations in a conduit-reservoir system, application to very long period (VLP) seismicity at basaltic volcanoes–Part I: Theory

Chao Liang[1], **Leif Karlstrom**[3], **and Eric M. Dunham**[1,2]

[1]Department of Geophysics, Stanford University
[2]Institute for Computational and Mathematical Engineering, Stanford University
[3]Department of Earth Sciences, University of Oregon

Key Points:

- Eigenmodes of coupled conduit-crack system explain VLP seismic events and crack wave resonances
- Conduit-reservoir mode with period of tens of seconds features magma oscillating in conduit with restoring force from buoyancy and reservoir stiffness
- Reduced model for conduit-reservoir mode connects VLP period and quality factor to geometry and magma properties and highlights parameter trade-offs

Corresponding author: Chao Liang, chao2@stanford.edu

Abstract

Very long period (VLP, 2-100 s) seismic signals at basaltic volcanoes like Kilauea, Hawai‘i, and Mount Erebus, Antarctica, are likely from resonant oscillations of magma within the shallow plumbing system. The system consists of conduits connected to cracks (dikes and sills) or reservoirs of other shapes. A quantitative understanding of wave propagation and resonance in a coupled conduit-crack system is required to interpret observations. In this work, we idealize the system as an axisymmetric conduit coupled to a tabular crack, accounting for fluid inertia, compressibility, and viscosity, gravity, and crack wall elasticity. We perform time-domain simulations and eigenmode analyses of the governing equations, linearized about a rest state. The fundamental mode or conduit-reservoir mode reflects the balance of conduit magma inertia with gravity (and, for small cracks, crack wall elasticity). Magma oscillates in an effectively incompressible manner within the conduit, deflating and inflating the crack, which couples to the surrounding solid to produce observable surface displacements. For sufficiently low viscosity magmas, viscous effects are confined to boundary layers. Shorter period modes are primarily reverberating crack waves with negligible coupling to the conduit. Finally, we introduce an approximate reduced model for the conduit-reservoir mode, which can also handle more general reservoir geometries (e.g., spherical chambers). The reduced model connects the observable VLP period and quality factor to two uniquely constrained parameters: the inviscid oscillation period T_0 and the viscous diffusion time τ_{vis} across the conduit radius. Our models can be extended to study the seismic response of more complex magmatic systems.

1 Introduction

Very long period (VLP) oscillations with periods in the range of 2-100 s are widely observed at active basaltic volcanoes, such as Kilauea Volcano, Hawai‘i [*Chouet et al.*, 2010; *Dawson et al.*, 2010; *Chouet and Dawson*, 2011; *Patrick et al.*, 2011; *Carey et al.*, 2012; *Chouet and Dawson*, 2013; *Orr et al.*, 2013; *Patrick et al.*, 2013; *Dawson and Chouet*, 2014] and Mount Erebus, Antarctica [*Rowe et al.*, 2000; *Mah*, 2003; *Aster et al.*, 2003, 2008; *Knox et al.*, 2018]. These remarkable oscillations are visible in the raw seismic data and can last for as long as 10 to 20 minutes before their amplitudes decay back to the noise level. They are thought to be triggered by the final expansion and burst of rising gas slugs [*Chouet et al.*, 2010; *Aster et al.*, 2003, 2008] and by rock falls onto the lava lake surface [*Patrick et al.*, 2011; *Carey et al.*, 2012, 2013; *Orr et al.*, 2013]. However, some VLPs can occur with no obvious manifestations on the lava lake surfaces [*Dawson and Chouet*, 2014] or at volcanoes with no lava lakes [*Waite*, 2014].

The VLP oscillations are commonly attributed to the resonance of waves in the magma plumbing system consisting of shallow conduits connected to reservoirs with various shapes, such as cracks or more equidimensional bodies (e.g., spheroids and ellipsoids). The distinct seismic signatures of VLP events, such as their periods, decay rates, and surface deformation pattern,s are crucial to inferring the geometry and fluid properties of the magmatic system. In a series of two papers, we investigate the resonance of waves in a coupled conduit-reservoir system in general (Part I, the current paper) and then apply that to interpret the VLP observations from Kilauea Volcano (Part II). A fluid-filled crack supports crack waves with phase velocities much lower than the fluid sound wave speed [*Krauklis*, 1962; *Staecker and Wang*, 1973; *Chouet*, 1986; *Ferrazzini and Aki*, 1987; *Korneev*, 2008; *Lipovsky and Dunham*, 2015; *Liang et al.*, 2017] and could interact with acoustic-gravity waves in the conduit [*Karlstrom and Dunham*, 2016]. Therefore, we devote primary efforts to investigate wave propagation in a conduit-crack system and then generalize to reservoirs of other shapes for the conduit-reservoir mode. The work initiated here marks one step toward physical models that account for wave propagation in both the conduit and reservoir and also connect the magma flow in a coupled conduit-reservoir system with seismic waves and deformation in the solid Earth.

To interpret the VLP observations, numerous oscillation models have been proposed. *Aster et al.* [2003] reviewed multiple possible oscillation mechanisms for Mount Erebus including trapped body waves, surface gravity waves, and oscillatory recharge driven by buoyancy in the conduit, and concluded that oscillation driven by the buoyancy in the conduit is the most viable explanation. However, *Aster et al.* [2003] neglect the restoring force from the magma reservoir. In addition, internal gravity waves in a stratified conduit deserve a more rigorous treatment. *Chouet and Dawson* [2013] proposed a lumped parameter model that advanced our understanding of VLP oscillations at Kilauea Volcano. In this model, fluid in the entire conduit oscillates, inflating and deflating a deeper reservoir. The VLP oscillation results from the balance of fluid inertia in the conduit and restoring force from the reservoir. However, the fluid compressibility and buoyancy in the conduit are neglected. *Chouet et al.* [2010] and *Chouet and Dawson* [2013] interpret the VLP source at Kilauea as a dual-dike system. These magma-filled cracks should support crack waves but their effects on VLP oscillations were not properly treated. In addition, the Poiseuille flow assumption in *Chouet and Dawson* [2013] does not account for viscous boundary layers that could develop near the conduit wall. Therefore, significant work remains to understand the resonant modes in a coupled conduit-crack system and the interplay between different restoring forces and inertia in such a system.

In this paper, we continue to explore the physics of VLP oscillations and reevaluate various assumptions made in the simplified models previously mentioned. We model wave propagation and resonance in the coupled conduit-crack system shown in Figure 1. The crack can be a sill or dike that serves as a shallow magma reservoir. We focus on the linearized dynamics of the system describing small perturbations about a rest state that is in mechanical (i.e., magmastatic) equilibrium but with general (other than thermodynamically stable) stratification. We start by deriving the governing equations and energy balance of the coupled system, capturing acoustic-gravity waves in the conduit following *Karlstrom and Dunham* [2016] and crack waves in the crack. Viscosity is rigorously treated both in the conduit following *Prochnow et al.* [2017] and in the crack following *O'Reilly et al.* [2017] and *Liang et al.* [2017]. A time domain simulation of a rock fall event is performed to reveal the magma flow, distribution of pressure, and seismic expressions of waves in the coupled conduit-crack system. We then proceed to characterize several important eigenmode types of the system (the conduit-reservoir mode and two types of crack wave modes) by analyzing their periods, decay rates, eigenfunctions (i.e., spatial distribution of magma velocity and pressure perturbations), and energetics. The eigenmode analysis motivates development of a reduced model for the conduit-reservoir mode by keeping fluid inertia, viscosity, and gravity in the conduit and elasticity from the crack, while neglecting other unimportant effects like fluid compressibility and wave propagation in the crack. We also extend the reduced model to more general reservoirs than a basal crack, such as spherical or ellipsoidal chambers. The validity of the reduced model and the sensitivity of the conduit-reservoir mode properties to various physical parameters are discussed in the appendix. We then connect the reduced model to observable VLP period and quality factor by identifying the parameter combinations that can be uniquely constrained from the seismic data. Finally, we discuss how individual parameters trade off with one another. This work serves as the theoretical foundation for a Bayesian inversion of the Kilauea VLP seismic data carried out in Part II.

2 Modeling approach

In this section, we derive the governing equations and the energy balance of the coupled conduit-crack model and briefly summarize the numerical methods used to solve the equations. Finally, we present results from a representative time domain simulation of a rockfall event.

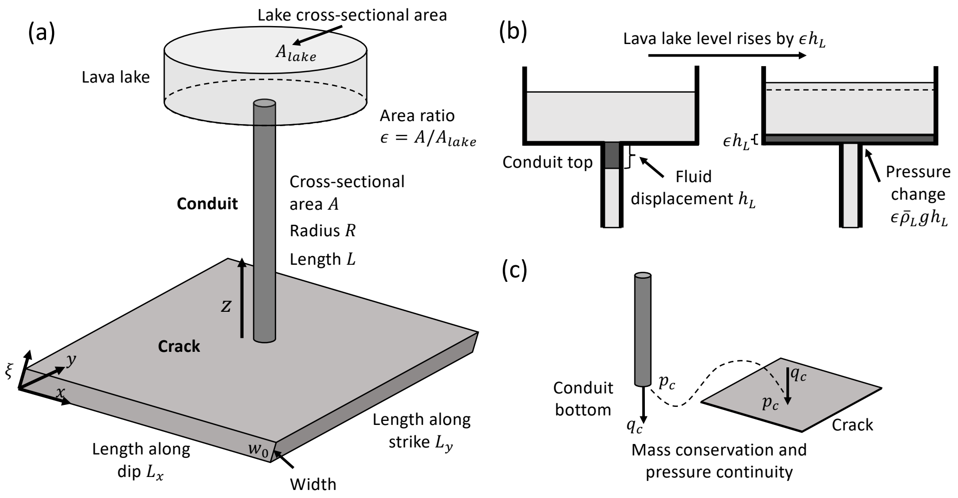

Figure 1. (a) Coupled conduit-crack system: a cylindrical conduit is connected to a tabular crack at the bottom and to a lava lake at the top. z denotes the direction along the conduit. The crack can be tilted and has its own coordinate system (x, y, and ξ). (b) Detail of coupling at the conduit top. Fluid with density $\bar{\rho}_L$ is exchanged with the lava lake from the conduit, which induces hydrostatic pressure change $\epsilon \bar{\rho}_L g h_L$ at the top of the conduit. (c) Detail of coupling at the conduit bottom where mass conservation and pressure continuity must be satisfied.

2.1 Governing equations in the conduit

We consider unsteady magma motions in a cylindrical conduit with constant radius filled with viscous stratified fluid. The bubble growth and resorption (BGR) considered by *Karlstrom and Dunham* [2016] is neglected. This implies that gas/liquid partitioning is in equilibrium over the time scales of interest. We also assume no relative flow between the gas and liquid phases. We first derive the governing equations for the unsteady motions and then perform the linearization with respect to a background state initially at rest. The energy balance is then derived by combining the governing equations with boundary conditions. Finally, the incompressible limit of the conduit model is presented.

2.1.1 Unsteady magma motions

Consider unsteady magma motions along a conduit with radius R and length L, as shown in Figure 1a. Derivation is first done for a vertical conduit and then generalized to a tilted conduit. By restricting attention to wavelengths much greater than the conduit radius, we treat fluid density $\tilde{\rho} = \tilde{\rho}(z,t)$ and pressure $\tilde{p} = \tilde{p}(z,t)$ as uniform in the radial direction and velocity $\tilde{v} = \tilde{v}(z,r,t)$ as being axisymmetric following *Prochnow et al.* [2017]. In this limit, the cross-sectionally averaged mass balance is

$$\frac{\partial \tilde{\rho}}{\partial t} + \frac{\partial (\tilde{\rho}\tilde{u})}{\partial z} = 0, \tag{1}$$

where t is time, z and r are the vertical (positive up) and radial coordinates, and

$$\tilde{u}(z,t) = \frac{1}{\pi R^2} \int_0^R \tilde{v}(z,r,t) 2\pi r dr \tag{2}$$

is vertical, cross-sectionally averaged fluid velocity. The vertical momentum balance is

$$\tilde{\rho}\left(\frac{\partial \tilde{v}}{\partial t} + \tilde{v}\frac{\partial \tilde{v}}{\partial z}\right) + \frac{\partial \tilde{p}}{\partial z} = \mu \frac{1}{r}\frac{\partial}{\partial r}\left(r\frac{\partial \tilde{v}}{\partial r}\right) - \tilde{\rho} g, \tag{3}$$

where μ is viscosity and g is gravitational acceleration. The above equations generalize in a straightforward manner to a tilted conduit by interpreting z as axial distance along the conduit and replacing g with $g\sin(\beta)$, where β is the dip angle of the conduit ($\beta = \pi/2$ is vertical). Since we treat magma as a single phase mixture, the change in bubble rise regime in tilted conduits [*James et al.*, 2004] and density wave oscillations in sub-horizontal conduits [*Fujita et al.*, 2011] are not considered.

The equation of state following a fluid parcel is

$$\frac{1}{\tilde{\rho}}\frac{D\tilde{\rho}}{Dt} = \frac{1}{K}\frac{D\tilde{p}}{Dt}, \tag{4}$$

where K is fluid bulk modulus and

$$\frac{D}{Dt} = \frac{\partial}{\partial t} + \tilde{u}\frac{\partial}{\partial z} \tag{5}$$

is the cross-sectionally averaged material derivative.

2.1.2 Linearization

To study the response to a small perturbation about a background state initially at rest, we write the total fields, denoted with a tilde, as the sum of the background values, denoted with an overbar, and perturbations:

$$[\tilde{v}, \tilde{u}, \tilde{p}, \tilde{\rho}] = [\bar{v}, \bar{u}, \bar{p}, \bar{\rho}] + [v, u, p, \rho]. \tag{6}$$

The static background state implies:

$$\bar{v} = \bar{u} = 0, \tag{7}$$

and

$$\frac{d\bar{p}}{dz} = -\bar{\rho}g. \tag{8}$$

Substituting (6) into (1), (3), and (4) and dropping higher order terms of perturbation fields, we obtain the linearized governing equations with p, v, and ρ as dependent variables:

$$\frac{\partial \rho}{\partial t} + u\frac{d\bar{\rho}}{dz} + \bar{\rho}\frac{\partial u}{\partial z} = 0, \tag{9}$$

$$\bar{\rho}\frac{\partial v}{\partial t} + \frac{\partial p}{\partial z} = \mu\frac{1}{r}\frac{\partial}{\partial r}\left(r\frac{\partial v}{\partial r}\right) - \rho g, \tag{10}$$

$$\frac{1}{\bar{\rho}}\left(\frac{\partial \rho}{\partial t} + u\frac{d\bar{\rho}}{dz}\right) = \frac{1}{K}\left(\frac{\partial p}{\partial t} + u\frac{d\bar{p}}{dz}\right), \tag{11}$$

where

$$u = \frac{1}{\pi R^2}\int_0^R v 2\pi r dr. \tag{12}$$

Rewriting (9) using (11) and (8), we have

$$\frac{1}{K}\frac{\partial p}{\partial t} + \frac{\partial u}{\partial z} = \frac{\bar{\rho}g}{K}u. \tag{13}$$

Using (8), we rewrite (11):

$$\frac{\partial}{\partial t}\left(\frac{\rho}{\bar{\rho}} - \frac{p}{K}\right) = Mu, \tag{14}$$

where

$$M = -\left(\frac{1}{\bar{\rho}}\frac{d\bar{\rho}}{dz} + \frac{\bar{\rho}g}{K}\right). \tag{15}$$

We define the fluid acoustic wave speed as

$$c = \sqrt{K/\bar{\rho}} \tag{16}$$

and the fluid displacement h as

$$\frac{\partial h}{\partial t} = u. \tag{17}$$

Substituting (17) in (14) and integrating in time, we have:

$$\frac{\rho}{\bar{\rho}} - \frac{p}{K} = Mh. \tag{18}$$

Using (18), we eliminate ρ in (10) and obtain

$$\bar{\rho}\frac{\partial v}{\partial t} + \frac{\partial p}{\partial z} = \mu\frac{1}{r}\frac{\partial}{\partial r}\left(r\frac{\partial v}{\partial r}\right) - \frac{p}{K}\bar{\rho}g - M\bar{\rho}gh. \tag{19}$$

Equations (13), (17), and (19) constitute another formulation of the governing equations with p, v, and h as dependent variables, which is similar to the governing equations in *Karlstrom and Dunham* [2016] after removing the non-equilibrium BGR process. The source of buoyancy in the conduit lies in the condition

$$M \neq 0. \tag{20}$$

The physical meaning of (20) can be understood by a thought experiment involving a fluid parcel in a vertically stratified fluid column initially at rest. The fluid parcel is perturbed and reaches a new position. Equation (20) implies that the change in background pressure expands/contracts the fluid parcel such that its density is different from the background density at the new position, resulting in non-zero net buoyancy [*Gill*, 1982]. Fluid parcel stably oscillates around the unperturbed position when $M > 0$ and accelerates unstably when $M < 0$. In a real volcanic conduit, the background state is a result of complex convection of multiphase fluids and solids, where $M = 0$ in general may not hold. In *Karlstrom and Dunham* [2016], the source of buoyancy is the non-equilibrium BGR process. In this study, we assume that the background state initially at rest is thermodynamically stable, which implies $M \geq 0$ but is not limited to the equality $M = 0$. The Brunt-Väisälä frequency N_b modified by compressibility is defined as

$$N_b = \sqrt{Mg}, \tag{21}$$

which can be expanded using (15):

$$N_b = \sqrt{-\frac{g}{\bar{\rho}}\frac{d\bar{\rho}}{dz} - \frac{\bar{\rho}g^2}{K}}. \tag{22}$$

In the case $M > 0$, N_b is thus the angular frequency of oscillation driven by buoyancy.

2.1.3 Boundary conditions

The momentum balance equation is supplemented with a no-slip boundary condition on the conduit wall:

$$v|_{r=R} = 0, \tag{23}$$

and the absence of mass source at $r = 0$ implies

$$\left.\frac{\partial v}{\partial r}\right|_{r=0} = 0. \tag{24}$$

At the bottom of the conduit, we assume that the fluid density is the same as that in the crack. Thus, the continuity of pressure and conservation of mass require

$$p|_{z=0} = p_c, \tag{25}$$

$$u|_{z=0} = -\frac{q_c}{A}, \tag{26}$$

where $A = \pi R^2$ is the conduit cross-sectional area, p_c is the fluid pressure in the crack at the location where the conduit and crack are coupled, and q_c is the volumetric flow rate into the crack from the conduit (with the minus sign arising from our convention that z and u are positive up).

The top of the conduit is connected to a lava lake with cross-sectional area A_{lake}, whose level fluctuates as lava enters or exits the lake through the conduit. In this study, we neglect the fluid dynamical processes within the lava lake. Instead, we assume that the lava lake adjusts to an equilibrium flat surface over time scales much shorter than the ones we are studying here and that the rate of fluid injection from the conduit is small such that the inertia of the fluid in the lake is negligible. The sloshing of fluid inside the lake and the viscous dissipation as fluid passes through the lake-conduit junction are not modeled. After making these assumptions, the fluctuation of the lava lake level is parameterized into the hydrostatic pressure change at the top of the conduit.

We model the excitation process by an external pressure $p_{ex}(t)$ applied at the top of the conduit. This $p_{ex}(t)$ should be understood as the pressure perturbation resolved at the top of the conduit by a complex mixture of reaction forces inside the lava lake induced by the rock fall impact, bubble bursting, and the viscous drag as the rock sinks in the lake. Therefore, the total pressure change at the top of the conduit due to both the external excitation and the fluctuation of lava lake level is

$$p = p_{ex} + \epsilon \bar{\rho}_L g h_L, \tag{27}$$

$$\frac{dh_L}{dt} = u_L, \tag{28}$$

where u_L and h_L are fluid cross-sectionally averaged velocity and displacement at the top of the conduit, $\epsilon = A/A_{lake}$ is the cross-sectional area ratio between the conduit and lava lake, and $\bar{\rho}_L$ is the fluid density at the top of the conduit. Note that for a tilted conduit all appearances of g are replaced by $g\sin(\beta)$ except in (27) because the lake walls are assumed to be vertical. When a large lava lake is present, such as the case at Kilauea, the area ratio $\epsilon \ll 1$ and the pressure perturbation induced by the fluctuating lava lake level is negligible. When the lava drains completely into the conduit, we have $\epsilon = 1$ and L is the length of the fluid column rather than the total length of the conduit.

2.1.4 Energy balance

We proceed to derive the energy balance in the conduit with the governing equations and boundary conditions. All the energies associated with the conduit (or the pipe) have a superscript *pipe* to differentiate with the energy terms in the crack, which are denoted with a superscript *crack*. We multiply (13) with Ap, and multiply (19) with v, integrate over the entire conduit and sum the two; then using (17) and boundary conditions (23)-(28), we have the energy balance

$$\frac{dE^{pipe}}{dt} = \frac{d}{dt}\left(\mathcal{K}^{pipe} + \mathcal{P}^{pipe}_{comp} + \mathcal{P}^{pipe}_{grav} + \mathcal{P}^{pipe}_{lake}\right) = -p_c q_c - p_{ex} u_L A - \dot{E}^{pipe}_{vis}, \tag{29}$$

where E^{pipe} is the total energy in the conduit, and

$$\mathcal{K}^{pipe} = \int_0^L \int_0^R \frac{\bar{\rho} v^2}{2} 2\pi r dr dz, \tag{30}$$

$$\mathcal{P}^{pipe}_{comp} = \int_0^L \frac{p^2}{2K} A dz, \tag{31}$$

$$\mathcal{P}^{pipe}_{grav} = \int_0^L \frac{\bar{\rho} g}{2} M h^2 A dz, \tag{32}$$

$$\mathcal{P}^{pipe}_{lake} = \frac{1}{2}\epsilon \bar{\rho}_L g_t A h_L^2, \tag{33}$$

$$\dot{E}_{vis}^{pipe} = \int_0^L \int_0^R \mu \left(\frac{\partial v}{\partial r}\right)^2 2\pi r dr dz \tag{34}$$

are the fluid kinetic energy, potential energy from fluid compressibility, gravitational potential energy from buoyancy, gravitational potential energy associated with the fluctuation of the top of the magma column, and rate of energy dissipation due to viscosity, respectively. The first two terms on the right hand side of (29) are the work rate done by the crack on the conduit as fluid is forced into or out of the conduit and the work rate from external pressure excitation, respectively. Equation (32) indicates that the condition $M = 0$ eliminates buoyancy.

2.1.5 Incompressible limit

In the limit where the fluid responds to perturbations in an effectively incompressible manner (c and $K \to \infty$), we have

$$M = -\frac{1}{\bar{\rho}}\frac{d\bar{\rho}}{dz}, \tag{35}$$

$$\rho = -\frac{d\bar{\rho}}{dz}h. \tag{36}$$

The governing equations (9), (10), and (11) reduce to

$$\frac{\partial u}{\partial z} = 0, \tag{37}$$

$$\bar{\rho}\frac{\partial v}{\partial t} + \frac{\partial p}{\partial z} = \mu\frac{1}{r}\frac{\partial}{\partial r}\left(r\frac{\partial v}{\partial r}\right) - \rho g, \tag{38}$$

$$\frac{\partial \rho}{\partial t} + u\frac{d\bar{\rho}}{dz} = 0. \tag{39}$$

In the incompressible limit, the cross-sectionally averaged fluid velocity u and displacement h are uniform along the conduit. Density change is solely a result of advection of the background density gradient. Substituting equation (36) into equation (38) and eliminating ρ, we have

$$\bar{\rho}\frac{\partial v}{\partial t} + \frac{\partial p}{\partial z} = \mu\frac{1}{r}\frac{\partial}{\partial r}\left(r\frac{\partial v}{\partial r}\right) + \frac{d\bar{\rho}}{dz}hg, \tag{40}$$

$$\frac{dh}{dt} = u. \tag{41}$$

Using (35) and (18), the energy balance is simplified:

$$\mathcal{P}_{comp}^{pipe} = 0, \tag{42}$$

$$\mathcal{P}_{grav}^{pipe} = \int_0^L \frac{\bar{\rho}g}{2}Mh^2 A dz = \frac{g}{2}h^2 A \int_0^L -\frac{d\bar{\rho}}{dz}dz = \frac{g}{2}h^2 A\left(\bar{\rho}_0 - \bar{\rho}_L\right). \tag{43}$$

Note that in the incompressible limit, $\mathcal{P}_{grav}^{pipe}$ only depends on the density contrast between the conduit bottom and top, not on the details of stratification. As we shall see, this limit turns out to be appropriate for the conduit-reservoir oscillation mode because fluid compressibility is negligible compared to gravity and the restoring force from the crack.

2.2 Governing equations in the crack

In the crack, we solve a simplified version of the linearized Navier-Stokes equations in 3D valid at wavelengths greater than the fracture width [*Lipovsky and Dunham*, 2015; *O'Reilly et al.*, 2017; *Liang et al.*, 2017], that accounts for fluid viscosity, inertia, compressibility. We assume quasi-static elastic response of the fracture walls. Quasi-static elasticity is justified as we are interested in the long-wavelength limit where crack wave phase velocity is much smaller than elastic wave speeds in the solid [*Krauklis*, 1962; *Staecker and Wang*, 1973; *Ferrazzini and Aki*, 1987; *Korneev*, 2008; *Lipovsky and Dunham*, 2015], making seismic wave radiation and elastodynamic stress transfer negligible. Fluid properties are assumed to be homogeneous in the crack.

2.2.1 Linearized equations

We consider a tabular crack with strike ϕ, dip θ, length along dip L_x, length along strike L_y, and centroid at east X_c, north Y_c, and depth Z_c with the origin defined at the lava lake position. The local coordinate system for computation is defined in x, y, and ξ, which are the coordinates along the dip, strike, and width directions, respectively. The origin of local coordinate system is defined at one corner such that x, y, and ξ of every point within the crack are non-negative, as shown in Figure 1a. We extend the governing equations in *Lipovsky and Dunham* [2015] by adding another crack length dimension:

$$\frac{1}{K_0}\frac{\partial p}{\partial t} + \frac{1}{w_0}\frac{\partial w}{\partial t} + \frac{\partial u_x}{\partial x} + \frac{\partial u_y}{\partial y} = \frac{q_c}{w_0}\delta(x - x_c)\delta(y - y_c), \tag{44}$$

$$\bar{\rho}_0\frac{\partial v_x}{\partial t} + \frac{\partial p}{\partial x} = \mu_0\frac{\partial^2 v_x}{\partial \xi^2}, \tag{45}$$

$$\bar{\rho}_0\frac{\partial v_y}{\partial t} + \frac{\partial p}{\partial y} = \mu_0\frac{\partial^2 v_y}{\partial \xi^2}, \tag{46}$$

where K_0, $\bar{\rho}_0$, and μ_0 are fluid bulk modulus, density, and viscosity in the crack, w_0 is the unperturbed crack width, w is the crack width perturbation, ξ is position perpendicular to the fracture plane, q_c is the volumetric flow rate of fluid injected from the conduit into the crack, $\delta(x - x_c)$ and $\delta(y - y_c)$ are the delta functions that restrict the mass injection from the conduit to a coupling point at (x_c, y_c), and

$$u_x(x, y, t) = \frac{1}{w_0}\int_0^{w_0} v_x(x, y, \xi, t)d\xi, \tag{47}$$

$$u_y(x, y, t) = \frac{1}{w_0}\int_0^{w_0} v_y(x, y, \xi, t)d\xi, \tag{48}$$

are the width-averaged velocities. Due to long wavelengths relative to crack width, pressure is effectively uniform across the crack width and viscous dissipation is only due to shear within the velocity profile across the crack width (ξ) direction. The system of equations are closed by bringing in one additional linear nonlocal equation (a discrete version given in the Appendix) relating pressure p and opening w from quasi-static elasticity for a homogeneous elastic half-space *Okada* [1992]. The elastic solid is specified by the shear modulus G and Poisson ratio ν_s.

2.2.2 Boundary conditions

We neglect the work done by the shear traction at the crack walls between the solid and the fluid. The shear traction on crack walls is neglected in calculating the solid response and the solid wall motion parallel to the crack plane is neglected in writing the no-slip condition for the fluid following *Lipovsky and Dunham* [2015]:

$$v_x(x, y, 0) = v_x(x, y, w_0) = v_y(x, y, 0) = v_y(x, y, w_0) = 0. \tag{49}$$

Both approximations are required for a self-consistent energy balance for the approximate equations. No flow is allowed in or out of the crack edge, which requires

$$u_x(0, y) = u_x(L_x, y) = u_y(x, 0) = u_y(x, L_y) = 0. \tag{50}$$

2.2.3 Energy balance

We multiply (44) with pw_0, multiply (45) with v_x, multiply (46) with v_y, integrate and sum the three equations, and apply boundary conditions (49) and (50):

$$\frac{dE^{crack}}{dt} = \frac{d}{dt}\left(\mathcal{K}^{crack} + \mathcal{P}^{crack}_{comp} + \mathcal{P}^{crack}_{elas}\right) = p_c q_c - \dot{E}^{crack}_{vis}, \tag{51}$$

where $p_c = p(x_c, y_c)$ is the pressure at the coupling location (x_c, y_c), and

$$\mathcal{K}^{crack} = \int_0^{L_x}\int_0^{Ly}\int_0^{w_0} \frac{1}{2}\bar{\rho}_0\left(v_x^2 + v_x^2\right) d\xi dy dx, \tag{52}$$

$$\mathcal{P}^{crack}_{comp} = \int_0^{L_x}\int_0^{Ly} \frac{1}{2K_0} p^2 w_0 dy dx, \tag{53}$$

$$\mathcal{P}^{crack}_{elas} = \int_0^{t}\int_0^{L_x}\int_0^{Ly} p\frac{\partial w}{\partial t} dy dx, \tag{54}$$

$$\dot{E}^{crack}_{vis} = \int_0^{L_x}\int_0^{Ly}\int_0^{w_0} \mu_0\left[\left(\frac{\partial v_x}{\partial \xi}\right)^2 + \left(\frac{\partial v_y}{\partial \xi}\right)^2\right] d\xi dy dx, \tag{55}$$

are the fluid kinetic energy, potential energy associated with fluid compressibility, work done by the fluid on the solid, and rate of energy dissipation due to viscosity, respectively. For an elastic solid with either traction-free or rigid exterior boundaries, the stress work can be identified as the elastic strain energy $\mathcal{P}^{crack}_{elas}$ [*Jaeger et al.*, 2009]. The first term on the right hand side of equation (51) is the work rate done by the injection from the conduit.

2.3 Total energy balance

Summing (29) and (51), we obtain the total energy balance of the coupled conduit-crack system:

$$\frac{dE}{dt} = \frac{d}{dt}(\mathcal{K} + \mathcal{P}) = -p_{ex}u_L A - \dot{E}^{pipe}_{vis} - \dot{E}^{crack}_{vis}, \tag{56}$$

where E is total energy and

$$\mathcal{K} = \mathcal{K}^{pipe} + \mathcal{K}^{crack}, \tag{57}$$

$$\mathcal{P} = \mathcal{P}^{pipe} + \mathcal{P}^{crack} = \mathcal{P}^{pipe}_{comp} + \mathcal{P}^{pipe}_{grav} + \mathcal{P}^{pipe}_{lake} + \mathcal{P}^{crack}_{comp} + \mathcal{P}^{crack}_{elas} \tag{58}$$

are the total kinetic energy and total potential energy. The change of total energy is driven by the work done by the external excitation and dissipation due to viscosity in the conduit and crack. The interplay of different restoring forces and inertia at different frequencies results in a rich spectrum of resonant modes.

2.4 Surface displacements

We assume quasi-static elasticity to calculate solid Earth surface displacement from the pressure perturbations and tractions in the plumbing system. This assumption is justified at sufficiently long periods $T \gg d/c_e$, where d is source-station distance and c_e is solid elastic wave speed [*Aki and Richards*, 2009]. At VLP periods and ~1-10 km source-station distance, the quasi-static terms in the elastic Green's function dominate. At shorter periods or larger source-station distances, the dynamic Green's function must be used. In addition, we only account for the opening dislocations on the crack in calculating surface displacements, neglecting contributions from pressures and shear tractions acting on the conduit and lava lake walls.

llll

Table 1. Material properties of a time domain simulation

Property	Symbol	Value	Unit
Conduit			
Conduit length	L	300	m
Conduit radius	R	5	m
Conduit dip	β	$\pi/2$	radian
Magma density at conduit top	$\bar{\rho}_L$	800	kg/m^3
Magma density at conduit bottom	$\bar{\rho}_0$	2000	kg/m^3
Scale height	α	327.41	m
Gravitational acceleration	g	10	m/s^2
Magma acoustic wave speed	c	1000	m/s
Magma viscosity	μ	50	Pa s
Area ratio	ϵ	0	–
Crack			
Coupling position in crack local coordinates	(x_c, y_c)	(1000, 1000)	m
Crack length in x direction	L_x	2000	m
Crack length in y direction	L_y	2000	m
Crack width	w_0	4	m
Magma acoustic wave speed	c_0	1000	m/s
Magma viscosity	μ_0	50	Pa s
Magma density	$\bar{\rho}_0$	2000	kg/m^3
Centroid locations (east, north, depth)	(X_c, Y_c, Z_c)	(0, 0, 1000)	m
strike	ϕ	0	radian
dip	θ	0	radian
Solid			
Shear modulus	G	22	GPa
Poisson ratio	ν_s	0.3	-
Observation point			
Observation location (east, north, depth)	$(X_{obs}, Y_{obs}, Z_{obs})$	(0, 1000, 0)	m

[a] unit "–" means it is non-dimensional.

2.5 Simulation of a rock fall event

In this section, we perform a time domain simulation of a rockfall event. Numerical methods for solving the governing equations are discussed in Appendix A: . We demonstrate how different waves are excited and propagate within the coupled conduit-crack system, and how the resonant modes are manifested in the displacements of the solid Earth surface. The simulation reveals the distribution of pressure and magma movement that corresponds to the VLP oscillations. The conduit and crack geometries used in the simulation are inspired by the inversion results of *Chouet and Dawson* [2011, 2013] for the Kilauea VLPs. We first introduce the parametrization of the source excitation and conduit background properties, and then discuss the results.

The source time function of the pressure excitation is parametrized as a Gaussian:

$$p_{ex}(t) = A_p \exp\left(\frac{-(t-t_c)^2}{2T_d^2}\right), \tag{59}$$

where A_p is amplitude, t_c is the time when the source time function reaches the peak, and T_d quantifies the source duration. T_d also controls the frequency content of the source time function. Smaller T_d results in a narrower Gaussian peak in the time domain and a wider spectrum in the frequency domain. A pressure excitation with much shorter duration that the VLP oscillation period is effectively an impulse:

$$p_{ex}(t) \approx P_{ex}\delta(t - t_c), \tag{60}$$

where $P_{ex} = \sqrt{2\pi}A_p T_d$. Since we deal with a linear system, the system response is proportional to the spectral amplitude of the source excitation at a particular frequency. Therefore, what really determines the system's free oscillation response to impulsive excitation is P_{ex}, not A_p or T_d individually. In our simulation, we set $T_d = 0.25$ s, $A_p = 0.2$ MPa, and $t_c = 5$ s. Note that although we use a Gaussian to mimic a rockfall event, the source time function can be completely general.

Although more general background properties in the conduit can be used [*Karlstrom and Dunham*, 2016], we parametrize the density and wave speed in the following way:

$$\bar{\rho}(z) = \bar{\rho}_L \exp[(L - z)/\alpha], \tag{61}$$

$$c(z) = c_0, \tag{62}$$

where c_0 is constant and

$$\alpha = \frac{L}{\ln\bar{\rho}_0 - \ln\bar{\rho}_L} \tag{63}$$

is the density scale height. The advantage of this parametrization is obvious by rewriting (15) using (16),

$$M = \frac{1}{\alpha} - \frac{g}{c_0^2}, \tag{64}$$

which shows constant M over the depth. α and c_0 need to be chosen such that $M \geq 0$ to guarantee thermodynamic stability. This parametrization gives great simplicity in controlling buoyancy. In addition, magma viscosity in the conduit is treated as constant and is the same as that in the crack. Magma density in the crack is assumed to be $\bar{\rho}_0$, the same as that at the bottom of the conduit. Key parameters used in the simulation are summarized in Table 1.

The simulation is performed for 200 seconds. In this demonstration, we set $\epsilon = 0$ to simulate the case where the cross-sectional area of the lava lake is much larger than that of the conduit. In Figures 2-4, we observe the superposition of multiple resonant modes, including the conduit-reservoir mode, crack wave modes, and conduit acoustic wave modes. The superposition obscures the observation of the crack wave modes but the conduit-reservoir mode and conduit acoustic wave modes are clearly observed.

Counter-propagating acoustic waves in the conduit form resonant standing waves. The fundamental acoustic resonance corresponds to the one with the longest wavelength ($2L = 600$ m) and period ($2L/c = 0.6$ s), which dominates pressure perturbation inside the conduit during the first 50 seconds, as shown in Figure 2c. This is confirmed by the conduit pressure distribution at t = 10 s when the crack behaves approximately as a zero-pressure perturbation boundary, as shown in Figure 3a-4. Despite the large amplitudes of pressure perturbations induced by acoustic waves, the velocity perturbation in the conduit is dominated by the conduit-reservoir mode with a period of 38.8 s, as shown in Figure 2b. In the conduit-reservoir mode, magma in the entire conduit moves up and down approximately uniformly, deflating and inflating the bottom crack, which effectively transfers the pressure perturbation in the crack to surface displacements, as shown in Figure 2. The conduit-reservoir mode is also manifested as the dominant peak of the displacement amplitude spectrum, as shown in Figure 4b. The uniformity of cross-sectionally averaged velocity in the conduit over depth indicates that the fluid compressibility is negligible during the VLP oscillation given the parameters explored here. However, the conduit-reservoir mode in this case is not driven primarily by the restoring force from the bottom crack reservoir, as argued by *Chouet and Dawson* [2013], but instead by buoyancy, as we shall

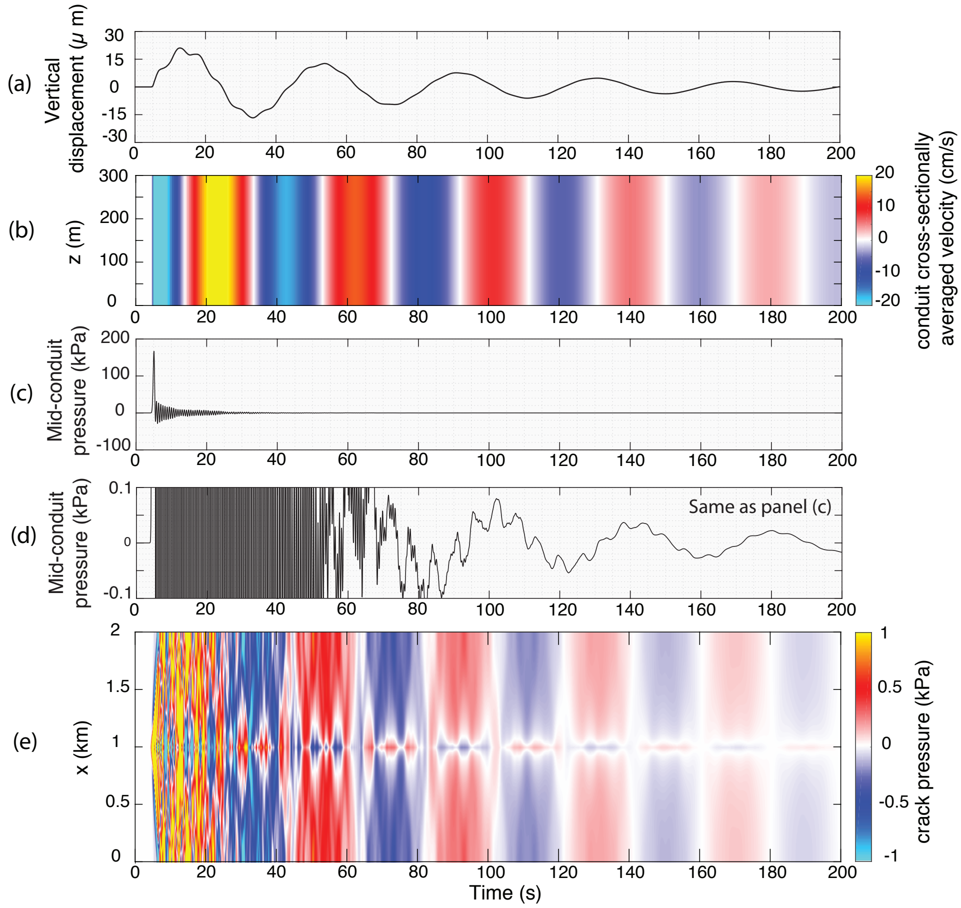

Figure 2. (a) Vertical surface displacement at an observational point 1 km north of the centroid of the crack. (b) Space-time plot of cross-sectionally averaged velocity in the conduit. Note that $z = 0$ denotes the bottom of the conduit. (c) Pressure at the middle point of the conduit. (d) Same as (c) with y-axis limit capped to reveal the VLP oscillation. (e) Space-time plot for crack pressure along x axis through the center of the crack.

see in the next section. As shown in Figures 3a-3 and 3b-3, narrow viscous boundary layers develop in both the conduit and crack, which highlights the importance of treating viscosity rigorously as opposed to simply assuming Poiseuille flow.

The pressure perturbations in the conduit induced by the conduit-reservoir mode are small and they are only visible after the resonating acoustic waves are gradually damped out by viscosity (after about 60 seconds), as shown in Figure 2d. Since the fluid compressibility is negligible for the conduit-reservoir mode, the pressure perturbations in the conduit are controlled by two factors: the dominant balance between buoyancy and inertia of magma in the conduit and the viscous drag on magma by the conduit wall. This can be understood by rewriting the incompressible limit of the conduit momentum balance (38) using (36) and integrating in the radial direction,

$$\frac{\partial p}{\partial z} = \left(-\bar{\rho}\frac{\partial u}{\partial t} + \frac{d\bar{\rho}}{dz}gh\right) + \frac{2\mu}{R}\left.\frac{\partial v}{\partial r}\right|_{r=R}.$$

The pressure distribution with depth can be reconstructed using the solutions of h and v with the boundary condition $p|_{z=L} = 0$. The good match between the reconstructed pressure distribution using (red dashed line) and the numerical simulation (black solid line) at

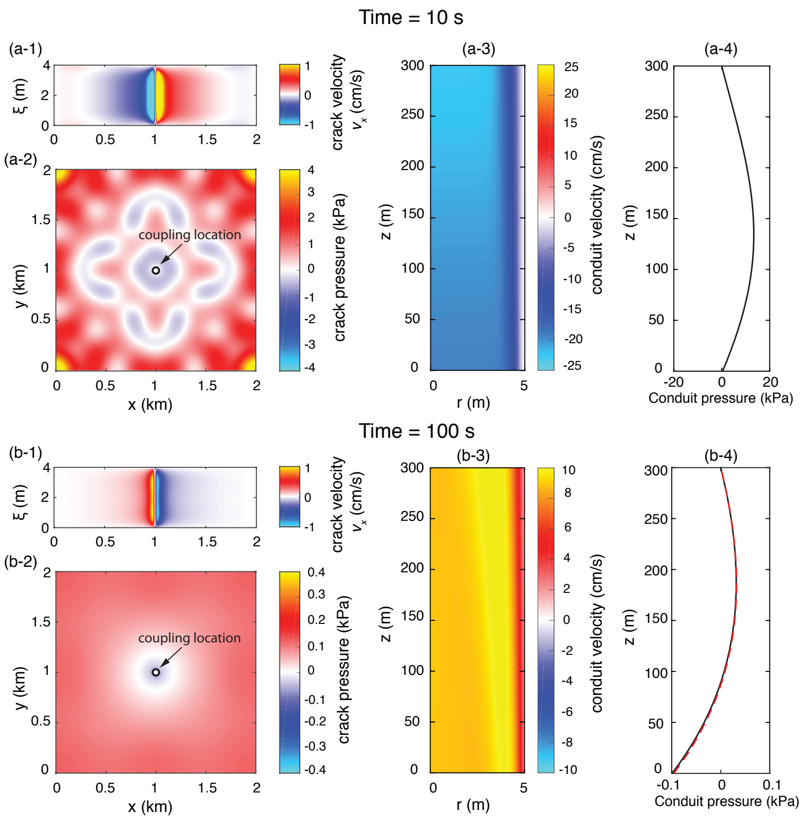

Figure 3. Snapshots of different fields at 10 s (a-1 to a-4) and 100 s (b-1 to b-4). (a-1) and (b-1) Fluid velocity v_x on a slice along the x direction cutting through the center of the crack. (a-2) and (b-2) Pressure distribution on the crack. Note that the color axis in (b-2) is saturated to reveal the pressure distribution at the later time. (a-3) and (b-3) Velocity distribution in the conduit. Viscous boundary layers develop near the conduit wall. (a-4) and (b-4) Pressure distribution along the conduit. The black solid lines are results from the numerical simulation. The red dashed line in (b-4) is the reconstructed conduit pressure distribution assuming incompressible flow.

t = 100 s shown in Figure 3b-4 indicates that the incompressible limit is a good approximation.

Acoustic waves in the conduit excite waves of varied wavelengths in the crack through the coupling point. Short-wavelength crack waves initially dominate the pressure perturbations in the crack and decay over time due to viscous dissipation, as shown in Figures 2e and 3a-2. However, similar to the conduit, the magma movement in the crack is dominated by long-wavelength crack wave modes and the conduit-reservoir mode, as shown in Figure 3a-1. Near the end of the simulation, waves along the crack are damped out and the conduit-reservoir mode dominates the pressure perturbation, which is approximately uniform except near the coupling location. Although various crack wave modes are superimposed in the time domain, the spectral amplitude of the surface displacement shown in Figure 4b reveals these resonances. Since the conduit is not capable of generating acoustic resonant modes with periods longer than 0.6 s, the spectral peaks with periods shorter than the conduit-reservoir mode but longer than 1 s shown in Figure 4b must be associated with crack waves, although only one mode (6.1 s) has sufficiently large amplitude to be visible in Figure 4a.

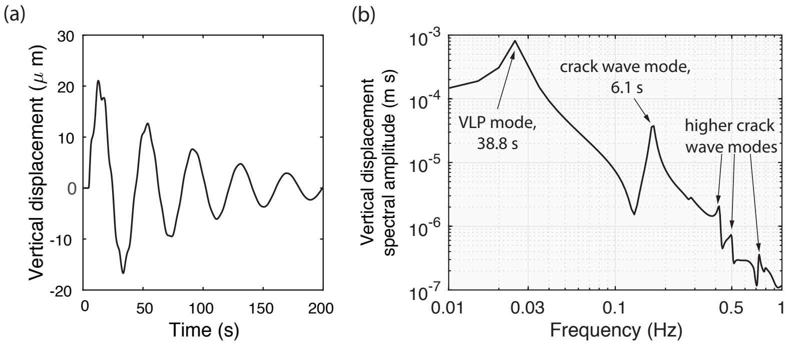

Figure 4. (a) Vertical surface displacement (a), replotted from Figure 2a, and (b) spectral amplitude at an observational point 1 km north of the centroid of the crack. The waveform is dominated by the conduit-reservoir mode (38.8 s) with a weaker long-period oscillation (6.1 s). Higher modes have negligible amplitudes compared to the first two modes.

In summary, we investigated the waves in a representative coupled conduit-crack system excited by a rock fall impact using time domain simulation. The surface displacement is dominated by the conduit-reservoir mode and a weaker crack wave mode. In the conduit-reservoir mode, the magma oscillates uniformly in the entire conduit, deflating and inflating the bottom crack. Short-wavelength crack waves are observed in the beginning of the simulation and decay in time. However, it is still unclear what is the primary restoring force for the conduit-reservoir mode and the percentage of inertia and viscous dissipation contributed by the crack. The superposition of different wave modes on the crack prevent the clear observations of individual modes in the time domain simulation. An eigenmode analysis is thus necessary to uncover the energy balance and fluid motion in each mode.

3 Eigenmode analysis

To gain a deeper physical understanding of each mode, we study the eigenmodes of the coupled conduit-crack system. Due to spatially varying properties in the conduit and finiteness of the crack, the eigenvalue problem must be solved numerically. We intend to demonstrate the types of eigenmodes that exist in the coupled conduit-crack system, rather than to obtain an exhaustive catalog of all the eigenmodes. Modes generally come in three families: conduit acoustic modes, crack wave modes, and the single-member conduit-reservoir mode. We focus on the conduit-reservoir mode but also briefly discuss the crack wave modes. Analysis in this section reveals the distinct energetics and spatial distributions of pressures and velocities of different eigenmodes in the coupled system, which also helps us further interpret the observed wave motions in the time domain simulation.

3.1 Method

We briefly summarize the method to solve the eigenvalue problem. After spatial discretization, the governing equations (13), (17), (19), (44), (45), and (46) without external forcing are reduced to a system of ordinary differential equations of the following form:

$$\frac{dU}{dt} = BU, \tag{65}$$

where matrix B contains the spatial discretization and enforcement of boundary conditions, and vector U contains the grid values of all the dependent variables (p, v, and h in the conduit and p, v_x, and v_y in the crack). The Laplace transform is defined as

$$\hat{F}(s) = \int_0^{+\infty} f(t)e^{-st}\,dt. \tag{66}$$

Taking the Laplace transform of equation 65, we have:

$$s\hat{U} = B\hat{U}, \tag{67}$$

where s is the eigenvalue of matrix B and $\hat{U}$ is the eigenvector. The complex eigenvalue s determines the resonant period

$$T = \frac{2\pi}{|\mathrm{Im}\ s|}, \tag{68}$$

and quality factor

$$Q = \frac{|\mathrm{Im}\ s|}{2|\ \mathrm{Re}\ s|}, \tag{69}$$

which is defined as the number of oscillations required for a free oscillating system's energy to fall off to $e^{-2\pi}$ or about 0.2% of its original energy [*Green*, 1955]. The quality factor is a metric of damping and the system is said to be overdamped when $Q < 0.5$ [*Hayek*, 2003].

We are only interested in oscillatory modes with nonzero Im s. As a consequence of energy stability, we have Re $s < 0$, which indicates energy dissipation. The eigenvector $\hat{U}$ determines spatial distribution of various fields, such as pressure, velocity, etc. Using the solution for $\hat{U}$, different energy terms can be calculated using (30), (31), (32), (52), (53), and (A.2). The rates of energy dissipation in the conduit and crack are calculated using (34) and (55). Analyzing the energetics reveals the sources of inertia and restoring forces that drive the oscillation, and the relative magnitude of viscous dissipation rates from the conduit and crack. Since the size of the matrix B increases dramatically when refining the mesh, we focus on analyzing the conduit-reservoir mode and a sample of long period crack wave modes using iterative methods with sufficient spatial resolution. We use the *eigs* function in Matlab to search for oscillatory modes with period longer than 1 s. Degenerate modes that share the same eigenvalue but have different eigenfunctions can exist. For example, if the crack has the same dimension in both the x and y directions and the conduit coupling location lies on a symmetry axis, the symmetry in x and y leads to degenerate modes. In this study, we search for solutions by specifying an initial guess of the eigenvalue/eigenfunction and examine just one of the degenerate modes, although one could overcome this limitation by starting with different initial guesses of eigenfunctions.

3.2 Eigenmodes

The energetics and eigenfunctions of the conduit-reservoir mode and two crack wave modes are shown in Figures 5, 7, and 9, respectively, with the surface displacement patterns shown in Figures 6, 8, and 10. The same parameters are used (Table 1) as the time domain simulation. The eigenfunctions are defined up a constant but the relative amplitudes of the different fields are uniquely defined. We normalize the real parts of similar fields in the conduit and crack with the same constant (the global maximum absolute value of real parts) so that we can compare the relative amplitudes. For example, we normalize the real parts of velocities with respect to the maximum absolute real values of all velocity fields (v, u, v_x, and v_y). Similar normalization is done for pressures in the conduit and crack.

3.2.1 The conduit-reservoir mode

The conduit-reservoir mode exemplified in Figure 5 is the mode with the longest period T and lowest quality factor Q, for the chosen model parameters. For the conduit-reservoir mode, oscillation of the entire magma column in the conduit is primarily driven

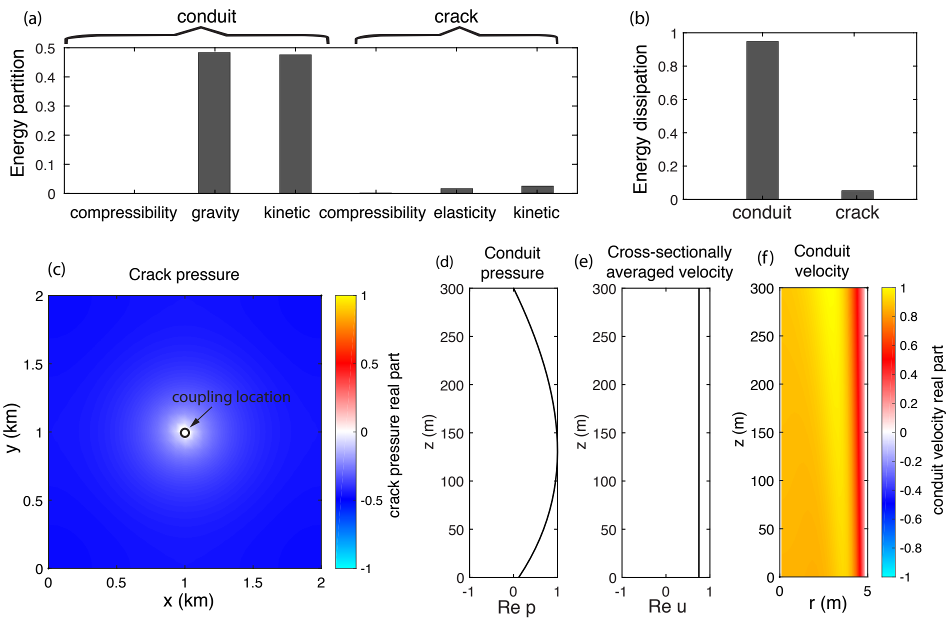

Figure 5. (a-b) Energetics and (c-f) real parts of eigenfunctions of the conduit-reservoir mode with a period of $T = 38.85$ s and a quality factor of $Q = 6.56$. The normalization scheme of eigenfunctions in (c-f) is described in the text. (a) Fractions of total energy contributed by different sources. Note the dominant balance between the fluid kinetic energy and gravitational energy in the conduit. Fluid compressibility is negligible. (b) Fraction of total energy dissipation. Note that most energy is dissipated in the conduit. (e) Approximately uniform distribution of velocity with depth. (f) Viscous boundary layers along the conduit walls.

by buoyancy with a small contribution from crack elasticity. This can be understood by realizing that the gravitational potential energy dominates among all potential energies, such as fluid compressibility and crack wall elasticity. However, the restoring force from crack wall elasticity can be substantial when the crack size is sufficiently small (Appendix B:). The kinetic energy primarily comes from the magma in the conduit. Most energy dissipation also occurs in the conduit, though more energy dissipation can occur in the crack as the crack width becomes sufficiently narrow (Appendix B:). Viscous boundary layers form near the walls of both the conduit and the crack, and the cross-sectionally averaged velocity in the conduit is approximately uniform along the depth direction as shown in figure 5-(e-f), which is consistent with the time domain simulation. Note that the eigenfunctions (Figure 5) and the snapshots of fields in the time domain simulation (Figure 3b) are not supposed to match exactly. The eigenfunctions have both real and imaginary parts, while we only plot the real parts. Also, the time domain simulation features the superposition of several modes. The analysis here together with the parametric study in Appendix B: motivates us to develop a reduced model for the conduit-reservoir mode in the next section, including conduit fluid inertia, gravity, and crack wall elasticity, but neglecting fluid compressibility and fluid inertia and dissipation in the crack.

3.2.2 Crack wave modes

Distinct from the conduit-reservoir mode, crack wave modes have energy confined primarily within the crack with negligible involvement of the conduit, as shown in Figures 7a and 7b. Fluid inertia in the crack is balanced by crack wall elasticity and also to a small extent by fluid compressibility, all of which are the defining features of crack waves. The contribution from fluid compressibility increases as the resonant frequency increases.

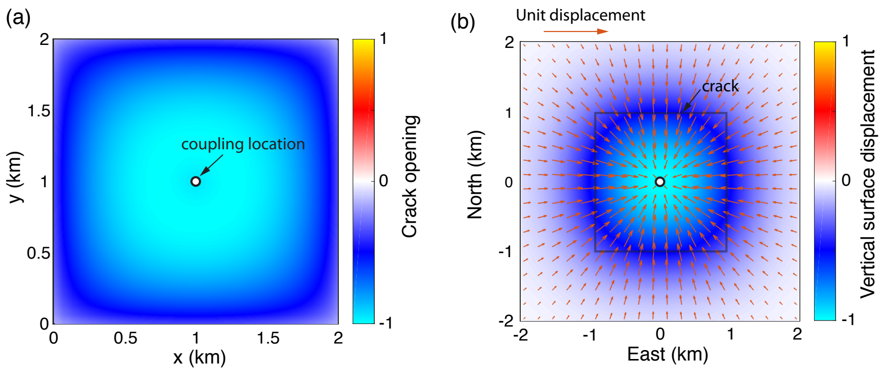

Figure 6. (a) Real part of crack opening normalized by the maximum absolute value and (b) normalized surface displacement of the conduit-reservoir mode. The vertical displacements are shown in color and the horizontal displacements are plotted as orange arrows in (b). The gray rectangle marks the spatial extent of the crack and the thick orange bar indicates the scale of unit displacement.

The confinement of energy within the crack is caused by the large hydraulic impedance contrast between the conduit and crack at the coupling point. At frequencies where the impedances of the conduit and crack match, energy is efficiently exchanged through the coupling junction, which permits the entire conduit and crack system to resonate [*Liang et al.*, 2017].

Depending on whether the conduit's coupling location is on a pressure nodal curve (zero pressure), two types of crack wave modes exist. In the first type, the coupling location is on a pressure nodal curve, locking all the energy and dissipation in the crack. An example of this type is shown in Figure 7 and has a period of 14.36 s. However, external forcing applied in the conduit necessarily induces pressure perturbation at the coupling location. As a result, this mode is not excited in the time domain simulation and no spectral peak is observed at 14.36 s in Figure 4b. In the other type, the coupling location is not on a pressure nodal curve and, in contrast to the 14.36 s period crack wave mode, a small amount of energy exists in the conduit. An example of this type is shown in Figure 9 and has a period of 6.1 s. The presence of a spectral peak at 6.1 s in Figure 4b indicates that this mode is excited in the time domain simulation though with a much smaller amplitude than the conduit-reservoir mode. Similar crack wave modes with higher frequencies, not explored in detail here, are also excited but the displacements induced by these higher modes are negligible at the observation point. This is because crack waves are interface waves and their disturbances to the solid decay exponentially with distance from the crack over a distance of order the crack wave wavelength. Therefore, crack wave modes with shorter wavelengths (or higher frequencies) induce much smaller surface displacements compared to long-wavelength modes.

3.2.3 Surface displacement pattern

As shown in Figures 6, 8, and 10, different eigenmodes exhibit distinct surface displacement patterns. For a horizontal crack, the conduit-reservoir mode generates vertical uplift/depression everywhere and horizontal expansion/contraction from the crack centroid due to the approximately uniform pressure distribution in the crack, as shown in Figure 6. However, crack wave modes can produce uplift at some locations and depression others. Large horizontal displacements can be generated at the boundary where the polarity of vertical displacements changes, as shown in Figure 8 and 10. Although crack orientation will modify the surface displacement pattern, the distinction of displacement patterns

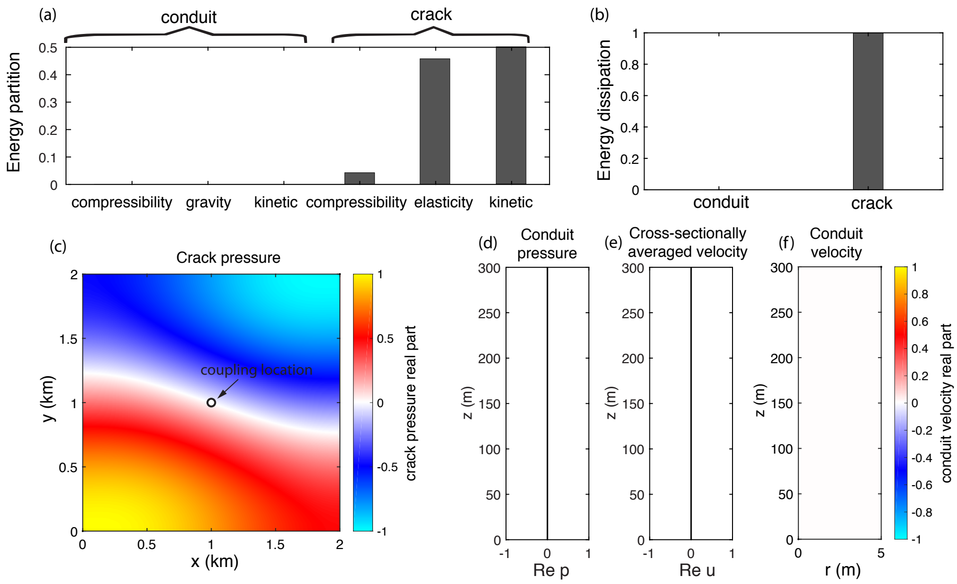

Figure 7. Same as Figure 5 but for a crack wave mode with period T = 14.36 s and quality factor Q = 10.66. Note the dominant balance between the fluid kinetic energy in the crack and elastic potential energy from the crack wall, which is the defining feature of crack waves. Energies and dissipations are sealed entirely in the crack because the coupling point is on a nodal curve of crack pressure (zero pressure). Note also the negligible fields in the conduit in (d-f).

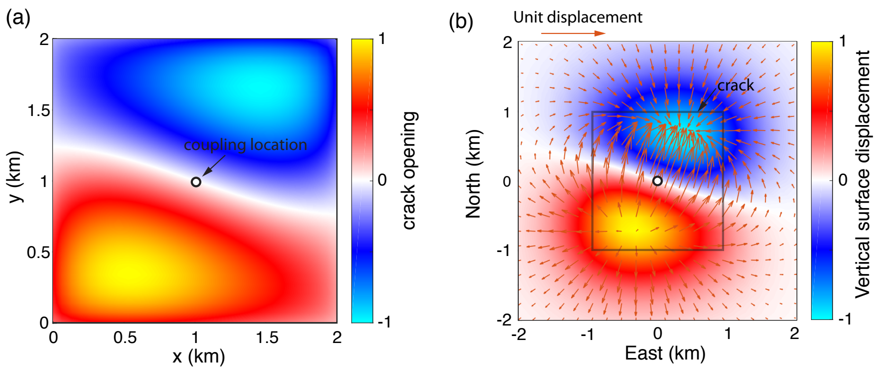

Figure 8. Same as Figure 6 but for a crack wave mode with period T = 14.36 s and quality factor Q = 10.66. Note the distinct displacement pattern compared to the conduit-reservoir mode shown in Figure 6.

among different eigenmodes should still exist. Thus, the surface displacement pattern of long period modes can help to constrain crack geometry.

4 Reduced model for the conduit-reservoir mode

Motivated by the eigenmode analysis in the previous section, we derive a reduced model for the conduit-reservoir mode, which includes conduit fluid inertia, gravity, and crack wall elasticity. Fluid inertia and viscous dissipation in the crack are neglected. The applicability of this reduced model is discussed in Appendix B: . Without viscous dissipation and fluid inertia inside the crack, the pressure perturbation inside the crack adjusts toward a uniform distribution over time scales much shorter than the conduit-reservoir

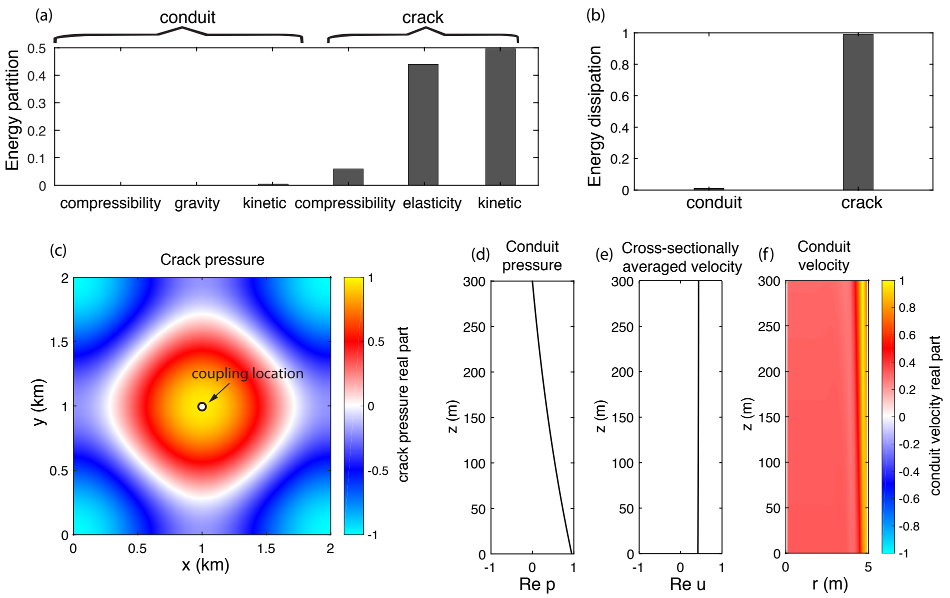

Figure 9. Same as Figure 5 but for a crack wave mode with period $T = 6.09$ s and quality factor $Q = 17$. In contrast to the crack wave mode shown in Figures 7 and 8, this crack wave mode couples to the conduit because the coupling point is located away from a nodal curve of crack pressure.

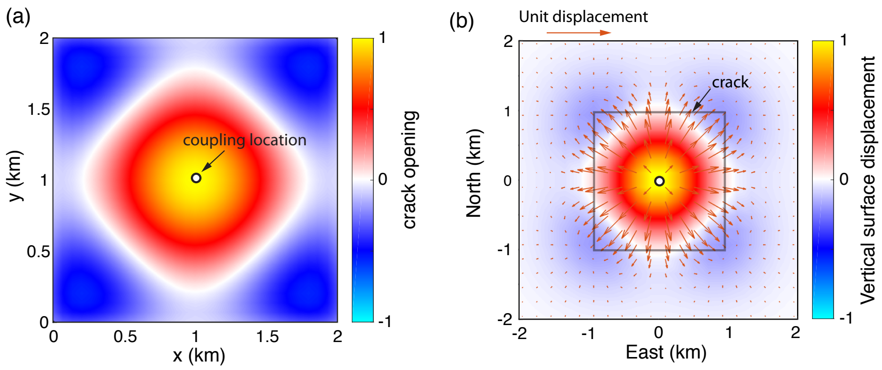

Figure 10. Same as Figure 6 but for a crack wave mode with period T = 6.09 s and quality factor Q = 17. Note the distinct displacement pattern compared to the conduit-reservoir mode shown in Figure 6 and the other crack wave mode shown in Figure 8.

mode period. In fact, this property also holds for magma reservoirs of other shapes, such as spherical or ellipsoidal chambers, as long as fluid inertia and viscous dissipation inside the magma reservoir can be neglected. With these approximations, the response of the entire magma reservoir can be lumped into a single restoring force quantified in terms of the overall stiffness of the reservoir. We first derive the governing equations for the reduced model in dimensional form, then cast them into nondimensional form. Finally, we connect key model parameters to observables (period and quality factor) and demonstrate how this model can be used to interpret VLP observations.

4.1 Governing equations

We now derive the governing equations for the reduced model. The equations to follow are stated explicitly for a conduit that dips at angle β. In the incompressible limit, we integrate (40) in z direction and rearrange terms, giving

$$\bar{\rho}_m \frac{\partial v}{\partial t} = -\frac{\bar{\rho}_0 - \bar{\rho}_L}{L} g \sin(\beta) h - \frac{1}{L}[p]_{z=0}^{L} + \mu \frac{1}{r}\frac{\partial}{\partial r}\left(r \frac{\partial v}{\partial r}\right), \tag{70}$$

where

$$\bar{\rho}_m = \frac{1}{L}\int_0^L \bar{\rho} dz \tag{71}$$

is the depth-averaged background density in the conduit. The fluid motion is driven by the change in weight of the entire conduit induced by advection of the density stratification and by the difference in pressure perturbation between the conduit top and bottom, and damped by viscosity. With fluid inertia and viscous dissipation neglected in the reservoir, the reservoir pressure change p_0 and conduit fluid displacement h are related by

$$p_0 = -C_t^{-1} A h, \tag{72}$$

where C_t is the total storativity, injected volume per unit pressure increase of the reservoir. In general, C_t is expressed as

$$C_t = (\beta_m + \beta_c)V, \tag{73}$$

where $\beta_m = \rho^{-1} d\rho/dp$ is magma compressibility, $\beta_c = V^{-1} dV/dp$ is the compressibility of the elastic reservoir, and $V = V(p)$ is reservoir volume. The compressibility for basaltic magma at reservoir depth ranges from 10^{-10} Pa^{-1} to 10^{-9} Pa^{-1} [e.g. *Rivalta and Segall*, 2008; *Anderson et al.*, 2015; *Mizuno et al.*, 2015]. The reservoir compressibility β_c depends on the shape of reservoir and solid rigidity G, which ranges from 1 to 30 GPa for volcanic areas [e.g. *Rivalta and Segall*, 2008].

For a penny-shaped crack [*Sneddon*, 1946],

$$V = \frac{\pi}{6} w_0 d_c^2, \tag{74}$$

$$\beta_c = \frac{2}{\pi G^*}\frac{d_c}{w_0}, \tag{75}$$

where $G^* = G/(1-\nu_s)$, d_c is the crack diameter, and w_0 is the crack width at the center. Given a crack with $d_c/w_0 \sim 100\text{–}1000$, we estimate β_c to be $2\times10^{-9}\text{–}1\times10^{-6}$ Pa^{-1}, which is much larger than β_m except for very stiff host rock ($G \sim 30$ GPa). We thus neglect magma compressibility in a crack-shaped reservoir and obtain

$$C_t = \frac{d_c^3}{3G^*} \tag{76}$$

for a penny-shaped crack. Note that the crack width w_0 does not affect C_t, which means the VLP oscillation is not sensitive to the crack width unless the viscous dissipation is dominant in the crack, as shown in Figure B.6. For a rectangular crack, similar scaling between C_t and crack length (L_x) exists:

$$C_t = \kappa \frac{L_x^3}{G^*}, \tag{77}$$

where the dimensionless coefficient κ depends on the aspect ratio of the crack and has to be calculated numerically.

For comparison, β_c of a spherical reservoir [e.g. *McTigue*, 1987] is $3/(4G)$, which is in the similar range as β_m. With a volume of $V = \pi d_c^3/6$ for a spherical chamber, we obtain

$$C_t = \frac{\pi d_c^3}{8G}(1 + 4\beta_m G/3), \tag{78}$$

accounting for both β_m and β_c.

Substituting the boundary conditions (27), (28), and (72) into (70), we have

$$\frac{\partial v}{\partial t} = -g'\frac{h}{L} + \nu_m \frac{1}{r}\frac{\partial}{\partial r}\left(r\frac{\partial v}{\partial r}\right) - \frac{p_{ex}}{\bar{\rho}_m L}, \tag{79}$$

where $\nu_m = \mu/\bar{\rho}_m$ is kinematic viscosity,

$$g' = (1+\gamma)\frac{\Delta\bar{\rho}}{\bar{\rho}_m}g \tag{80}$$

is reduced gravity modified by reservoir elasticity,

$$\Delta\bar{\rho} = (\bar{\rho}_0 - \bar{\rho}_L)\sin(\beta) + \epsilon\bar{\rho}_L \tag{81}$$

quantifies the density contrast driving gravitational restoring forces, and

$$\gamma = \frac{A}{C_t \Delta\bar{\rho} g} \tag{82}$$

is the dimensionless parameter that measures the relative magnitude of the restoring forces from the reservoir and gravity. When the lava lake area is large compared to the conduit cross-sectional area ($\epsilon \ll 1$) and the conduit is vertical, $\Delta\bar{\rho} \approx (\bar{\rho}_0 - \bar{\rho}_L)$ is simply the density contrast between the bottom and top of the conduit. When the lava lake is drained completely into the conduit ($\epsilon = 1$), the top of the magma column in the conduit is in direct contact with air, which gives $\Delta\bar{\rho} = \bar{\rho}_0$ for a vertical conduit. When $\gamma \gg 1$ the restoring force from the reservoir dominates the oscillation, and when $\gamma \ll 1$ gravity is the dominant restoring force. Since the reservoir is represented by C_t in the oscillation model, it is insufficient to determine the shape of the reservoir solely from the period and quality factor. To differentiate the reservoir shape, additional constraints from the surface displacement pattern, as discussed in the previous section, are required.

In the inviscid limit ($\nu_m = 0$), equation (79) is reduced to an undamped harmonic oscillator after setting external forcing p_{ex} to zero:

$$\frac{d^2h}{dt^2} + g'\frac{h}{L} = 0, \tag{83}$$

which gives the inviscid natural frequency ω_0 and period T_0:

$$\omega_0 = \sqrt{g'/L}, \tag{84}$$

$$T_0 = 2\pi\sqrt{L/g'}. \tag{85}$$

Figure 11 shows γ and T_0 at different reservoir dimension d_c and G for both crack-shaped and spherical reservoirs. Both increasing d_c and decreasing G can reduce γ and bring the resonant period closer to that of the purely gravity-driven oscillation ($\gamma = 0$). The C_t and γ of sufficiently small spherical chambers are influenced by magma compressibility β_m (assumed to be 10^{-9} Pa^{-1} in Figure 11).

4.2 Nondimensionalization

We nondimensionalise (79) and (17) by introducing the following dimensionless quantities:

$$t^* = t/\sqrt{L/g'}, \quad h^* = h/L, \quad r^* = r/R, \tag{86}$$

$$v^* = v/\sqrt{Lg'}, \quad u^* = u/\sqrt{Lg'}, \quad p^*_{ex} = p_{ex}/(\bar{\rho}_m g' L). \tag{87}$$

The nondimensionalised equations are

$$\frac{\partial v^*}{\partial t^*} = -h^* + \chi\frac{1}{r^*}\frac{\partial}{\partial r^*}\left(r^*\frac{\partial v^*}{\partial r^*}\right) - p^*_{ex}, \tag{88}$$

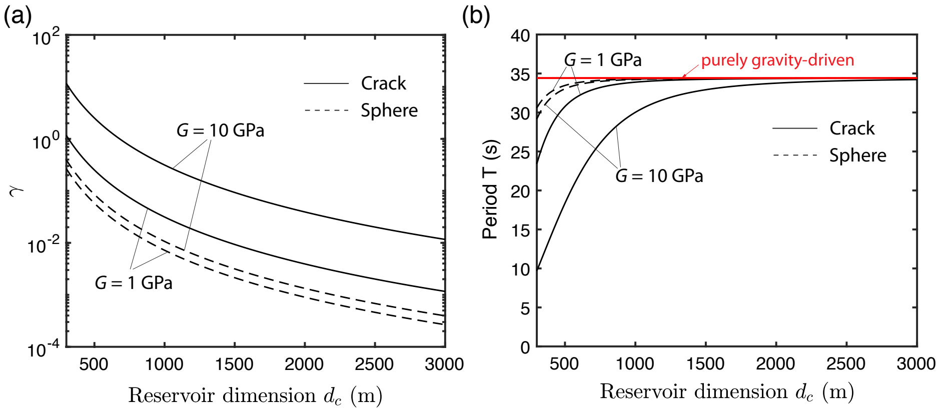

Figure 11. (a) Dimensionless parameter γ and (b) inviscid resonant period T_0 for different reservoir dimensions d_c, shear modulus G, and shapes (penny-shaped crack and sphere). Note that the oscillation approaches the purely gravity-driven limit as d_c increases and C_t increases. The conduit is assumed to be vertical. Parameters are $R = 5$ m, $L = 300$ m, $\Delta\bar{\rho} = 1000$ kg/m^3, $\bar{\rho} = 1000$ kg/m^3, $\nu_s = 0.25$, and $\beta_m = 10^{-9}$ Pa^{-1}.

$$\frac{dh^*}{dt^*} = u^*, \tag{89}$$

$$u^* = 2\int_0^1 v^* r^* dr^* \tag{90}$$

where

$$\chi = \frac{\sqrt{L/g'}}{R^2/\nu_m} = \frac{T_0/2\pi}{\tau_{vis}} \tag{91}$$

is a ratio between two time scales: the period of inviscid oscillation T_0 and the diffusion time across the conduit radius

$$\tau_{vis} = R^2/\nu_m. \tag{92}$$

4.3 Results

Here, we present the theoretical results from solving the dimensionless model equations (88), (89), and (90). We identify the two parameter combinations that can be uniquely constrained by the observations of VLP periods and quality factors and discuss the trade-offs between individual parameters.

Being the only dimensionless parameter in (88), χ determines the dynamics of the free oscillation system, as shown in Figure 12. When $\chi \approx 1$, the oscillation time scale is long enough that the viscous boundary layer is able to fully develop across the conduit radius, achieving the Poiseuille flow. In fact, even when $\chi = 0.1$, the quality factor is only 1.3 and the velocity profile to close to parabolic. When $\chi \ll 1$, shear strain is confined in a narrow boundary layer close to the conduit wall. Greater χ signifies more viscous damping and, as a result, leads to lower quality factor and slightly longer period. The viscous oscillation period T deviates less than 10% from the inviscid oscillation period T_0 when Q is larger than 5, and this deviation increases substantially as χ approaches the limit of being overdamped. At Kilauea, the observed Q for the conduit-reservoir mode ranges from 5 to 40 [*Dawson and Chouet*, 2014], which reveals the range of χ to be 0.003-0.01. Therefore, a proper treatment of viscous boundary layers in the conduit is crucial for correctly capturing the decay characteristics of the VLP oscillation in that system.

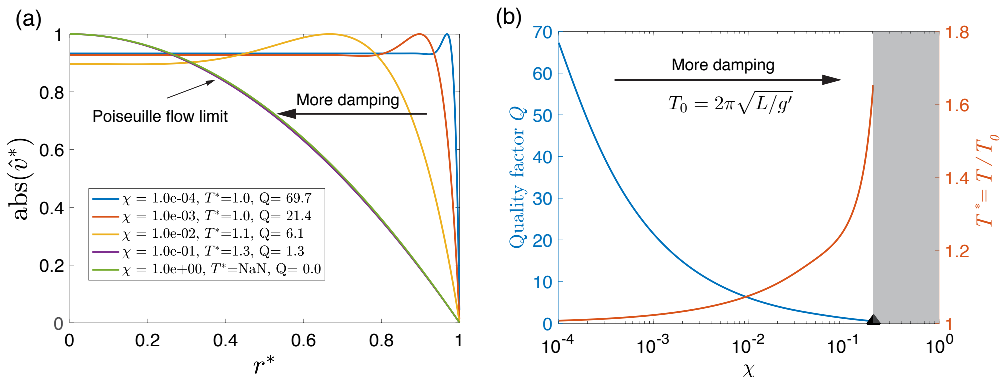

Figure 12. (a) Velocity eigenfunction $\hat{v}^*$ (normalized by the maximum value) with different values of χ. Increasing χ marks the transition from boundary layer flow to Poiseuille flow. (b) Quality factor Q and nondimensional period T^* at different values of χ. Greater χ signifies more viscous damping, resulting in lower Q and longer T^*. The dark gray region marks the overdamped region ($Q < 0.5$).

During a forced oscillation, the system response is amplified at the resonant frequency. To visualize this effect, we solve for the spectrum of h^* given unit input of p^*_{ex} for a range of χ. The results are shown in Figure 13. Amplification is observed as spectral peaks at resonant frequencies ($\omega/\omega_0 \approx 1$) in Figure 13a. A higher quality factor Q (smaller χ) corresponds to a sharper spectral peak. Figure 13b shows the peak spectral amplitudes of h^* as a function of χ at the resonant frequency, which also indicates the suppression of amplification effect at a higher χ.

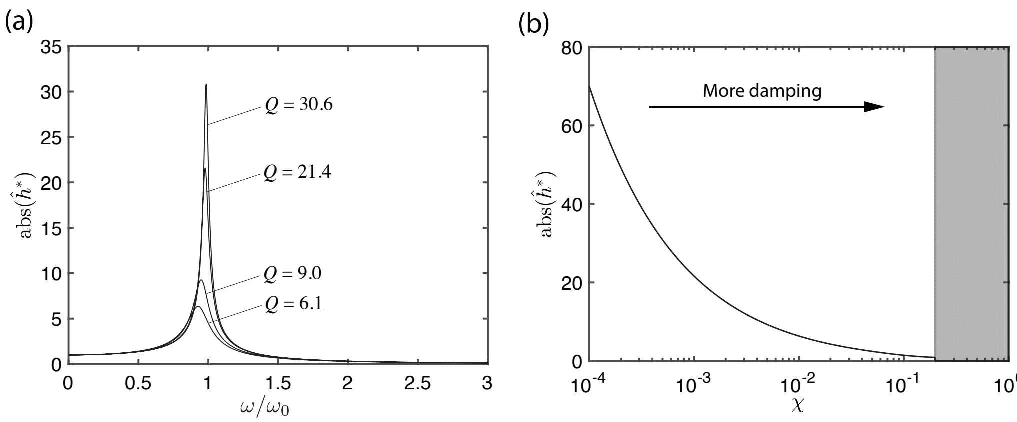

Figure 13. (a) Spectral amplitude of h^* as a function of ω/ω_0 given unit p^*_{ex}. The spectral peak indicates the amplification at the resonance; the higher the quality factor Q (the lower the χ), the sharper the spectral peak. (b) Peak spectral amplitude of h^* at resonant frequency as a function of χ. A higher χ indicates stronger damping and less amplification. The dark gray region marks the overdamped region ($Q < 0.5$).

What can we uniquely constrain given observations of period T and quality factor Q of a conduit-reservoir mode VLP event? Given two observations, only two parameters can be constrained in principal. Solutions in Figure 12b directly link the observed Q to the value of the nondimensional parameter χ. χ is then used to constrain $T^* = T/T_0$. Given T and T^*, T_0 is then uniquely constrained. Therefore, the two parameters uniquely constrained by the observation of T and Q are T_0 and τ_{vis}. This also means the individual parameters that constitute the expression of T_0 in equation 85 and τ_{vis} in (92) must have trade-offs given the limited observation.

When seismic displacements are available, they provide additional constraints. In the quasi-static limit, the surface displacement spectra $\hat{U}$ (not to be confused with the dependent variable vector U in (65) and with caret now denoting Fourier transform instead of Laplace transform) are proportional to the volume change in the reservoir [e.g. *Mogi*, 1958; *Okada*, 1985]:

$$\hat{U} = n_e A\hat{h} = n_e A\hat{h}^* L = n_e \frac{\hat{h}^*}{\hat{p}^*_{ex}} A\hat{p}^*_{ex} L = n_e \frac{\hat{h}^*}{\hat{p}^*_{ex}} \frac{A\hat{p}_{ex}}{\bar{\rho}_m L\omega_0^2}, \tag{93}$$

where n_e is a function of the reservoir location, station location, reservoir shape, relative magma and reservoir compressibilities, and elastic properties of the solid. Since ω_0 can be calculated from T_0 and h^*/p^*_{ex} is known from χ (see Figure 13), surface displacements thus constrain $A\hat{p}_{ex}/(\bar{\rho}_m L)$ if n_e is known.

According to (92), there is trade-off between the conduit radius R and the kinematic viscosity ν_m. Figure 14a shows this trade-off for $T_0 = 40$ s and different values of Q. If we have independent constraints on kinematic viscosity, we can put tighter constraints on the conduit radius, as indicated by the two dashed lines in Figure 14-(a) for a range of dynamic viscosity (1-100 Pa s) and background density (1000-2500 kg/m^3). However, it is not possible in general to uniquely constrain R and ν_m just from observations of T and Q. At Kilauea Volcano, forward looking infrared (FLIR) imagery in late 2008 to early 2009 reveals that the conduit radius is about 5 m on the floor of the Overlook crater at Kilauea Volcano [*Fee et al.*, 2010]. If we assume the measurement at the lake bottom is representative for the deeper conduit, we take R = 5 m. By using (92) and making reasonable assumptions of average background density ($\bar{\rho}_m$ ranges from 1000 to 2500 kg/m^3), we map out the relation between dynamic viscosity μ_m and Q given different observations of T_0, shown in Figure 14b. Given T_0 and $\bar{\rho}_m$, observing a greater Q indicates lower dynamic viscosity in the magma. With the observation of T_0 and Q, the viscosity can be bounded considering a range of density, which can be useful for monitoring the magma viscosity in the conduit. Higher quality factor provides a narrower bound on viscosity. For example, given $T_0 = 40$ s and $Q = 10$, the range of viscosity is bounded to 18-40 Pa s given the range of density (1000 to 2500 kg/m^3).

Similarly, a trade-off between conduit length L and reduced gravity g' also exists on observing the same T_0. To uncover the trade-offs between more physical parameters, we expand (85) using (80) and (82):

$$T_0 = 2\pi \sqrt{\frac{L\bar{\rho}_m}{\Delta\bar{\rho}g + AC_t^{-1}}}, \tag{94}$$

which clearly reveals the balance between the conduit fluid inertia ($L\bar{\rho}_m$) with two sources of restoring forces, one from gravity ($\Delta\bar{\rho}g$) and the other from reservoir (C_t).

To visualize the trade-off, we consider two limiting cases: one with zero density contrast $\Delta\bar{\rho} = 0$ and a crack-shaped reservoir considered by *Chouet and Dawson* [2011, 2013] (Figure 15a), and the other with infinite reservoir storativity $C_t \rightarrow +\infty$ (Figure 15b). In the first case, shown in Figure 15a, there exists a direct trade-off between the conduit length and crack radius. To sustain the same resonant period T_0, a shorter conduit is required for a larger crack. If the crack size is indeed as large as 3 km as reported by *Chouet and Dawson* [2011, 2013], the conduit would have to be less than 10 m long regardless of different average density and T_0 if no gravity is considered, which seems very unlikely. If the conduit is longer than 100 m, the crack diameter would have to be less than ~800 m given T_0 = 20 s and $\bar{\rho}_m$ = 1000 kg/m^3. A larger density would require an even smaller crack. In this calculation, we assume G = 20 GPa and ν_s = 0.25. A more

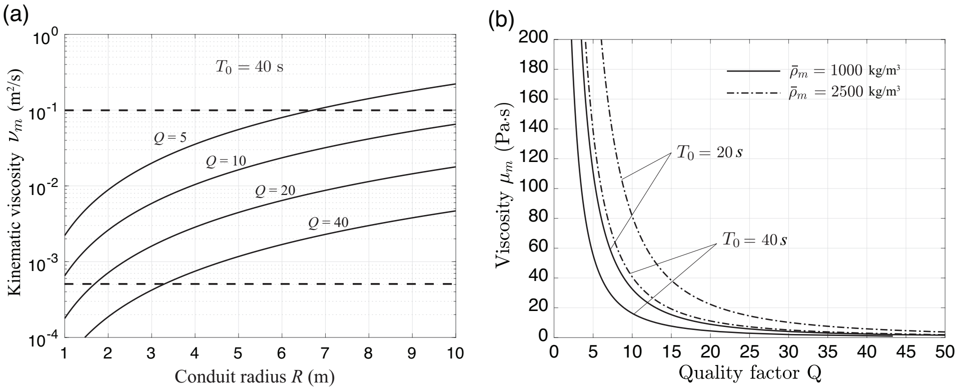

Figure 14. (a) Trade-off between kinematic viscosity ν_m and conduit radius R for different values of Q when T_0 is 40 s. The two black dashed lines indicate the bounds on kinematic viscosity if we bound the dynamic viscosity in the range of 1-100 Pa s and background density to 1000-2500 kg/m^3. (b) Average dynamic viscosity μ_m as a function of observed quality factor Q given different T_0 and different average background density $\bar{\rho}_m$. The conduit is assume to be vertical with radius R = 5 m.

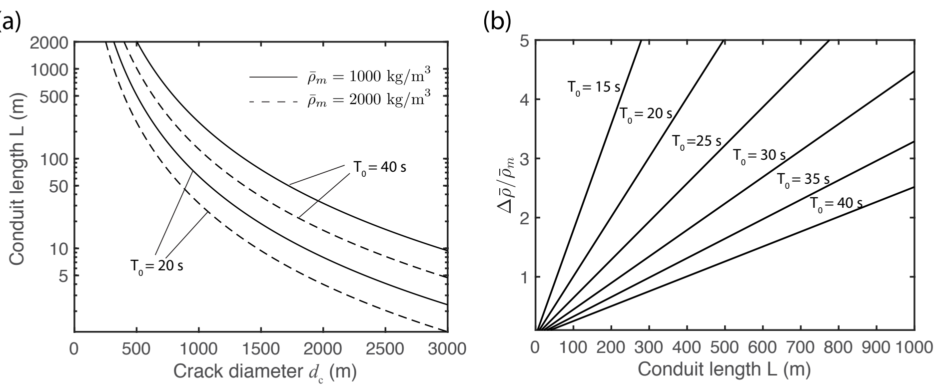

Figure 15. (a) Trade-off between conduit length L and crack diameter d_c (assuming a penny-shaped crack) given different $\bar{\rho}_m$ and T_0. Gravity is assumed to be zero ($\Delta\bar{\rho}$ = 0). (b) Trade-off between $\Delta\bar{\rho}/\bar{\rho}_m$ and L given different T_0. C_t is assumed to be $+\infty$. Calculations are performed assuming a vertical conduit with R = 5 m, G = 20 GPa, and ν_s = 0.25. Note that $\bar{\rho}_m$ is not assumed to be any specific value in (b). A higher ratio between density contrast $\Delta\bar{\rho}$ and average density $\bar{\rho}_m$ is required to produce the same period T_0 for a longer conduit.

compliant solid will also require a smaller crack. Therefore, if the crack size is as large as reported by *Chouet and Dawson* [2011], gravity must play the dominant role. In the second case, shown in Figure 15b, the oscillation is completely driven by gravity and the trade-off exists between $\Delta\bar{\rho}/\bar{\rho}_m$ and L. For the same period T_0, a larger density ratio $\Delta\bar{\rho}/\bar{\rho}_m$ is required for a longer conduit. Without the restoring force from the magma reservoir, the fact that we observe periods as short as 15-20 s requires the length of the conduit to be shorter than 300 meters assuming the density ratio $\Delta\bar{\rho}/\bar{\rho}_m$ is less than 5. The reality is probably somewhere in between the two limiting cases, as we explore in Part II.

5 Conclusion

We have investigated waves and resonant magma oscillations in a coupled conduit-crack system. Stratification and compressibility in the conduit support acoustic-gravity waves. Along the fluid-filled crack, solid wall elasticity and fluid inertia produce crack waves. Viscous boundary layers in both the conduit and crack are properly captured. Eigenmode analysis of the coupled model reveals distinct energy balance of a variety of resonant modes. The conduit-reservoir mode is characterized by the dominant balance of conduit fluid inertia, gravity, and crack wall elasticity. In this mode, the entire fluid column in the conduit moves up and down, inflating and deflating the bottom reservoir. Fluid compressibility is negligible and the contribution from the crack wall elasticity diminishes as the size of the crack gets larger. Unless the crack width is too narrow compared to the conduit radius, most energy is dissipated in the conduit. Due to the negligible magma compressibility as compared to buoyancy in the conduit, the conduit-reservoir mode is only sensitive to the average magma density and density contrast, not to the detailed density profile in conduit. Higher frequency modes are resonating crack waves with most energy confined in the crack. Depending on where the conduit couples to the crack, crack wave modes can be selectively excited by the external excitation in the conduit. Crack wave modes are visible in the surface displacement but their amplitudes are smaller than the conduit-reservoir mode. Distinct displacement patterns of crack wave modes may help to constrain the crack geometry.

The coupled model also led us to a reduced model that retains the key physics of the conduit-reservoir mode, which may explain certain VLP events at basaltic volcanoes. The advantage of our approach compared to previous ones is that we started from a very general model, which provides the reduced model with rigorous theoretical justifications. Since the conduit-reservoir mode senses the magma reservoir as a whole, its period and quality factor lose sensitivity to the shape of the reservoir except when that shape affects the storativity C_t. The reduced model led us to identify the key nondimensional parameter χ governing the oscillation and two parameters (T_0 and τ_{vis}) that can be uniquely constrained by observation of the VLP period T and quality factor Q. Trade-offs thus exist among the individual parameters that constitute T_0 and τ_{vis}. For example, direct trade-offs exist between kinematic viscosity and conduit radius, and between conduit length and density contrast. Our analysis also demonstrates that gravity is likely the dominant restoring force for conduit-reservoir mode VLP oscillations at Kilauea, rather than reservoir elasticity, as suggested by *Chouet and Dawson* [2013]. The sensitivity of T and Q to the intrinsic properties of the magmatic system complement the interpretation of the commonly obtained VLP seismic moment tensor in the literature [e.g. *Ohminato et al.*, 1998; *Chouet et al.*, 2010].

While the full model developed in this paper is general, the reduced model of the conduit-reservoir mode does have its range of application. In this study, we focus on the parameter values where there exists a clear separation of resonant frequencies among the conduit-reservoir mode, crack wave modes, and conduit acoustic wave modes. There might be cases where these modes' frequencies are comparable, which may complicate the interpretation. Future work might explore the impact of other processes not considered in this study, such as irregular conduit geometry [e.g. *Garces*, 2000], bubble growth and resorption [e.g. *Karlstrom and Dunham*, 2016], and background flow in the conduit [e.g. *Fowler and Robinson*, 2018] on the observables from seismograms. The conduit-reservoir model introduced in this work can furthermore serve as one component of more complex models of magma plumbing systems. Some extensions include coupling the conduit to multiple cracks, modeling gas rising and bursting in the lava lake, and treating the sloshing dynamics of the lava lake. These more complex models would give deeper physical insights on the resonances of the entire plumbing system and be more capable in assimilating diverse datasets, such as the seismic observations of higher modes, degassing observations, and infrasound signals.

Acknowledgments

This work was supported by the National Science Foundation (EAR-1624431). We thank Josh Crozier for assistance with seismic data and Ossian O'Reilly for help with numerics. The source code for the general conduit-crack model is available at `https://github.com/chaovite/crack_pipe`. The source code for the reduced model for the conduit-reservoir mode is available at `https://github.com/chaovite/conduit_reservoir_oscillator`.

A: Numerical methods

We solve (13), (18), and (19) in the conduit with p, v, and h as dependent variables and (44), (45), and (46) in the crack with p, v_x, v_y as dependent variables. We use summation-by-parts (SBP) finite difference methods for spatial discretization with weak enforcement of boundary conditions and coupling conditions via simultaneous approximation terms (SAT) [*Kreiss and Scherer*, 1974; *Strand*, 1994; *Olsson*, 1995]. The advantage of the SBP-SAT method is that it enables us to construct numerical energy balance that mimics the continuous energy balance and to prove the energy stability and accuracy of the numerical scheme. The SBP-SAT treatment of the conduit is explained in *Karlstrom and Dunham* [2016] (with no viscosity) and *Prochnow et al.* [2017] (with viscosity). The numerical treatment of the crack is identical to that in *O'Reilly et al.* [2017] except replacing elastodynamics in the solid with static elasticity and extending the crack to 3D. Specifically, we capture the static elasticity using the displacement discontinuity method (DDM) for an elastic half space [*Crouch et al.*, 1983; *Okada*, 1985, 1992] and the grid values of crack pressure $\mathbf{p}$ and opening $\mathbf{w}$ on a mesh are related by

$$\mathbf{p} = K_G \mathbf{w}, \tag{A.1}$$

where K_G is a symmetric positive-definite matrix due to reciprocity for linear elasticity. Thus, a discrete version of elastic potential energy (54) is:

$$\mathcal{P}^{crack}_{elas} = \frac{1}{2}\mathbf{p}^T H K_G^{-1} \mathbf{p}, \tag{A.2}$$

where H is the positive-definite diagonal SBP quadrature rule for integration in the x and y directions. After spatial discretization, we obtain a system of ordinary differential equations (ODE), which are integrated in time using a fourth-order implicit-explicit (IMEX) Runge-Kutta method following *O'Reilly et al.* [2017]. The stiffness induced by viscosity is handled implicitly so that the entire system of equations can be advanced in time with high order accuracy using the maximum time step determined by the standard Courant-Friedrichs-Lewy (CFL) condition for wave propagation.

B: Sensitivity analysis for the conduit-reservoir mode

In this section, we consider the special case of a rectangular crack with equal side lengths $L_x = L_y$ and discuss the sensitivity of period T, quality factor Q, and partition of energy of the VLP mode to conduit length L, conduit radius R, conduit density contrast $\bar{\rho}_0 - \bar{\rho}_L$, crack dimension L_x, crack width w_0, and viscosity μ. Fluid wave speed is not varied in this section because we expect the fluid compressibility to be negligible compared to gravity at very long periods. Due to the high dimension of the parametric space, an exhaustive study of each combination of parameters is impractical. Therefore, we vary one parameter at a time while holding other parameters fixed at the values of the reference model, tabulated in Table 1.

The results are shown in Figures B.1-B.6. We calculate T and Q for the full model without reduction, the reduced model with crack wall elasticity, and the reduced model without crack wall elasticity, which allows us to evaluate applicability of the reduced model. With the eigenfunctions obtained for the full model, we calculate the fractions of

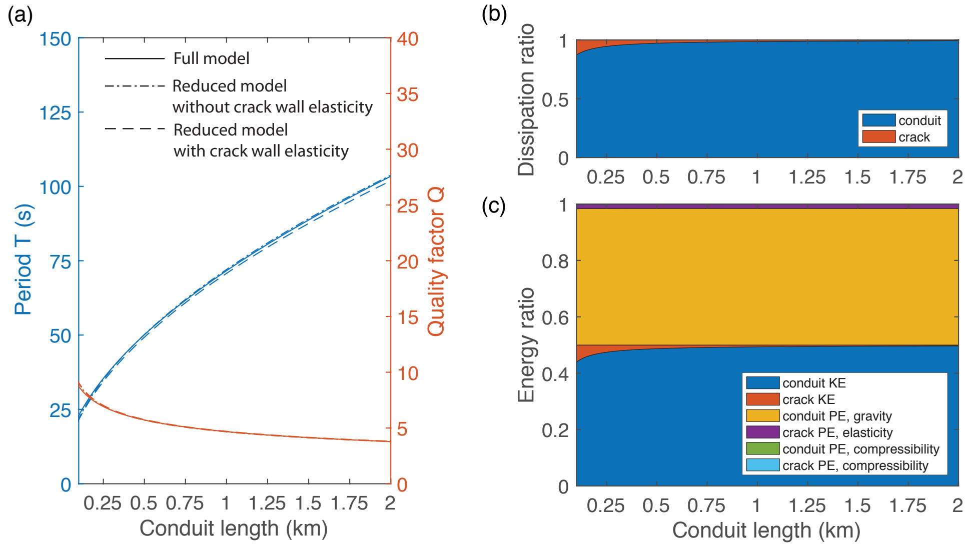

Figure B.1. (a) Conduit-reservoir mode period T (blue lines) and quality factor Q (red lines), (b) partition of energies, and (c) partition of energy dissipations as a function of conduit length. In (c), PE denotes potential energy and KE denotes kinetic energy.

total energy for all energy terms in the conduit and crack: fluid kinetic energy (30), potential energy due to fluid compressibility (31), and gravitational potential energy (32) in the conduit and fluid kinetic energy (52), potential energy due to fluid compressibility (53), and elastic potential energy (A.2) in the crack. We also calculate the fractions of total energy dissipation in the conduit (34) and the crack (55).

The most pronounced feature of the conduit-reservoir mode is the balance between fluid kinetic energy, the gravitational potential energy in the conduit, and crack wall elastic potential energy, which is important only when the crack dimension is sufficiently small. The period increases with conduit length and decreases with density contrast, as shown in Figures B.1 and B.2. Additional restoring force added by the crack wall elasticity further reduces the period, which becomes evident as the crack dimension is less than several hundred meters as shown in Figure B.3a. In the short crack limit, potential energy due to crack wall elasticity accounts for a substantial percentage in the total potential energy shown in Figure B.3c. Viscous dissipation tends to increase the period as shown in Figure B.4. However, this effect is modest until the system is close to being overdamped, such as when the conduit radius and crack width become too narrow, as shown in Figures B.5a and B.6a.

Higher viscosity, narrower conduit radius and crack width all contribute to a lower quality factor, according to Figures B.4, B.5, and B.6. The quality factor is not sensitive to the crack width when the crack width is sufficiently large and most energy is dissipated in the conduit. However when the crack width is sufficiently narrow that it becomes the limiting factor for the viscous dissipation; decreasing the crack width can dramatically decrease the quality factor, eventually approaching the limit of being over-damped, as shown in Figure B.6a.

In most cases, the period and quality factor are well approximated by the solutions from the reduced model (equation (79)). The reduced model accounting for crack wall elasticity slightly and consistently underestimates the period. This is because this solution includes the restoring force from elasticity but neglects the fluid inertia in the crack. This treatment is analogous to having a stiffer spring but a smaller mass, which consistently

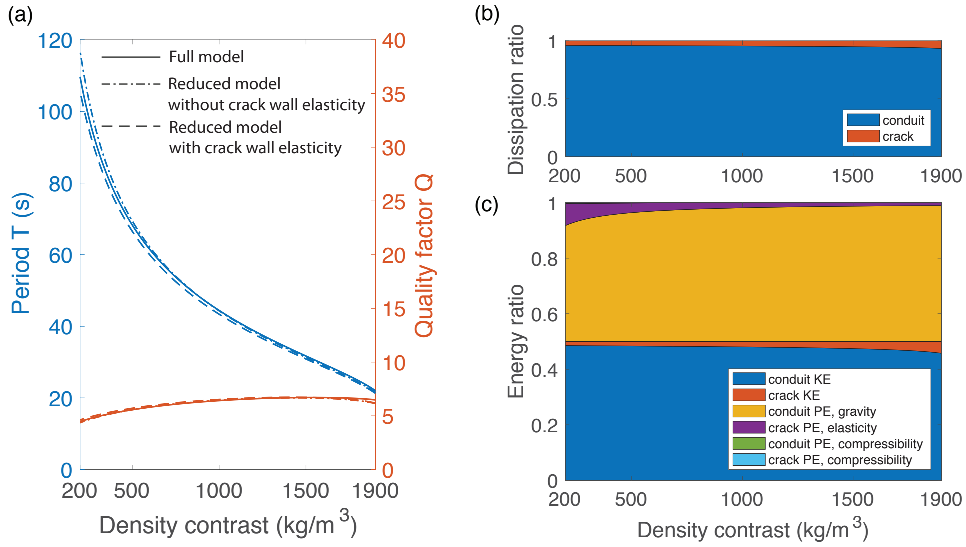

Figure B.2. Same as Figure B.1 but varying density contrast.

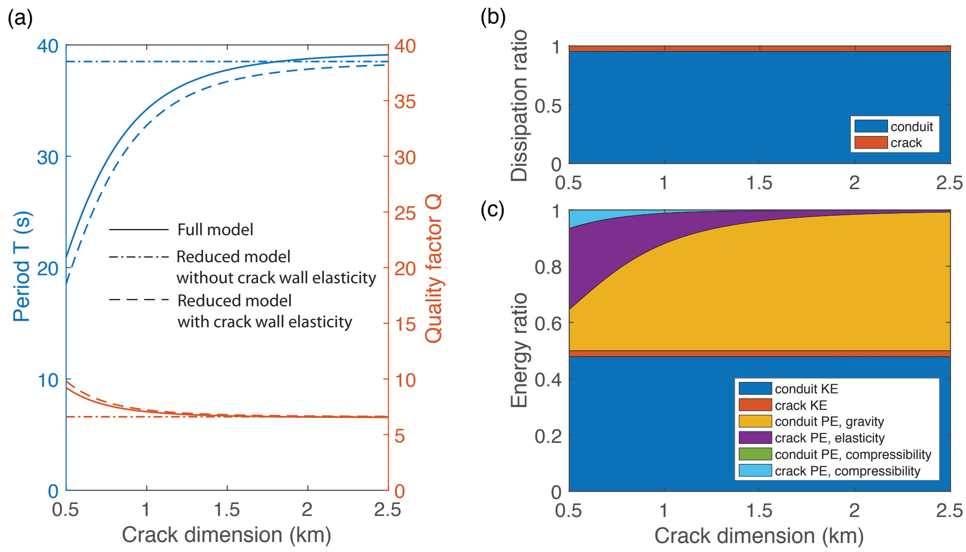

Figure B.3. Same as Figure B.1 but varying crack dimension.

gives a lower period. The reduced model with a zero pressure boundary condition (without including crack wall elasticity) neglects both crack wall elasticity and fluid inertia in the crack. In the case where the crack elasticity is approximately balancing the fluid inertia in the crack, this treatment gives a better approximation to the period and quality, as shown in Figures B.1, B.5, and B.4. However, neglecting the crack wall elasticity when it contributes a substantial part of the restoring force can induce large error, as shown in Figure B.3. Since reduced models neglect viscous dissipation in the crack, they break down when substantial viscous dissipation occurs in the crack, such as the cases where the conduit radius becomes sufficiently large or the crack width becomes sufficiently narrow, as shown in Figure B.5 and B.6.

To summarize, we have shown that the conduit-reservoir mode is dominated by the balance of conduit fluid inertia with the gravity and crack wall elasticity. The strength of

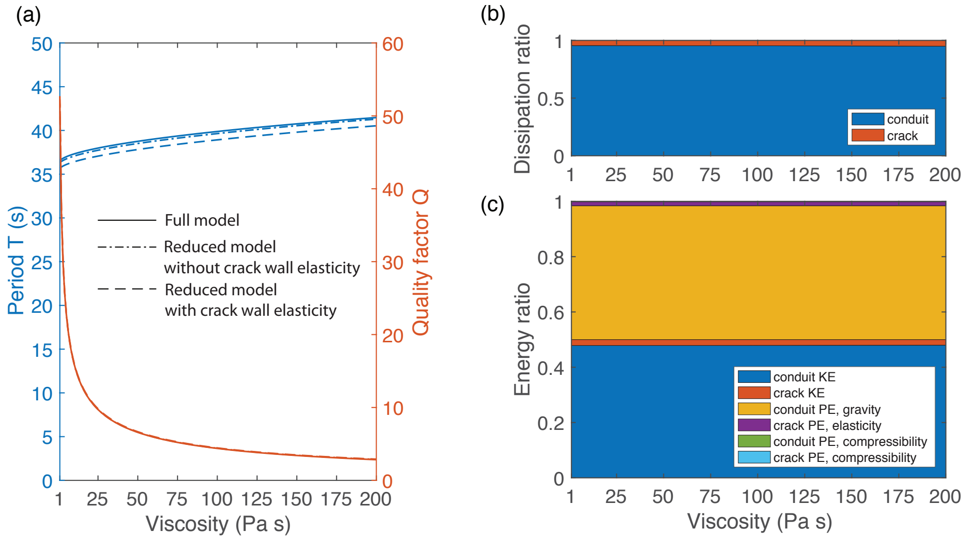

Figure B.4. Same as Figure B.1 but varying viscosity.

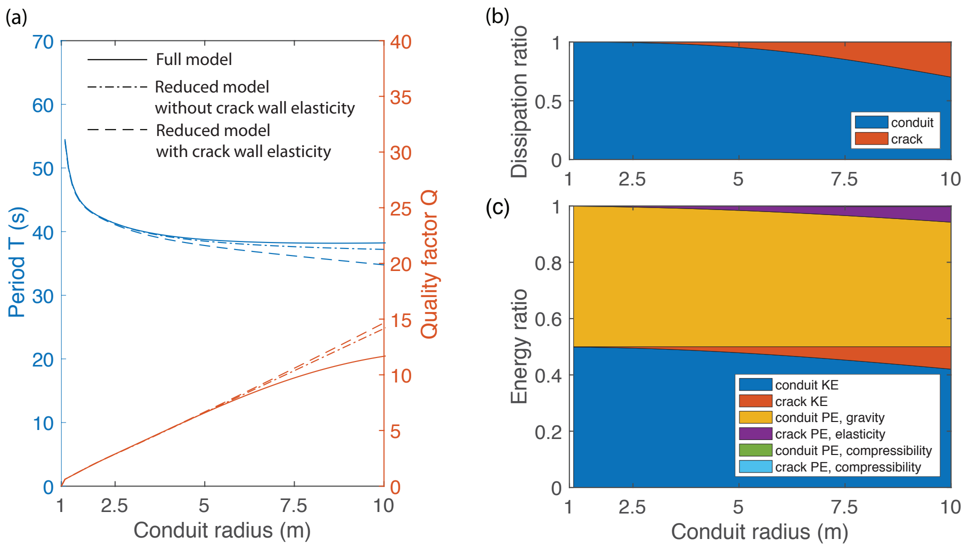

Figure B.5. Same as Figure B.1 but varying conduit radius

the crack wall elasticity diminishes as the crack size becomes sufficiently large. The fluid compressibility in both the conduit and crack is negligible. Most fluid inertia and viscous dissipation are concentrated in the conduit unless the crack width is sufficiently narrow, which justifies our decision to neglect the fluid inertia and viscosity in the crack in our reduced model for the conduit-reservoir mode.

References

Aki, K., and P. G. Richards (2009), *Quantitative Seismology*, University Science Books.

Anderson, K. R., M. P. Poland, J. H. Johnson, and A. Miklius (2015), *Episodic Deflation-Inflation Events at Kīlauea Volcano and Implications for the Shallow Magma System*, chap. 11, pp. 229–250, American Geophysical Union (AGU), doi:10.1002/9781118872079.ch11.

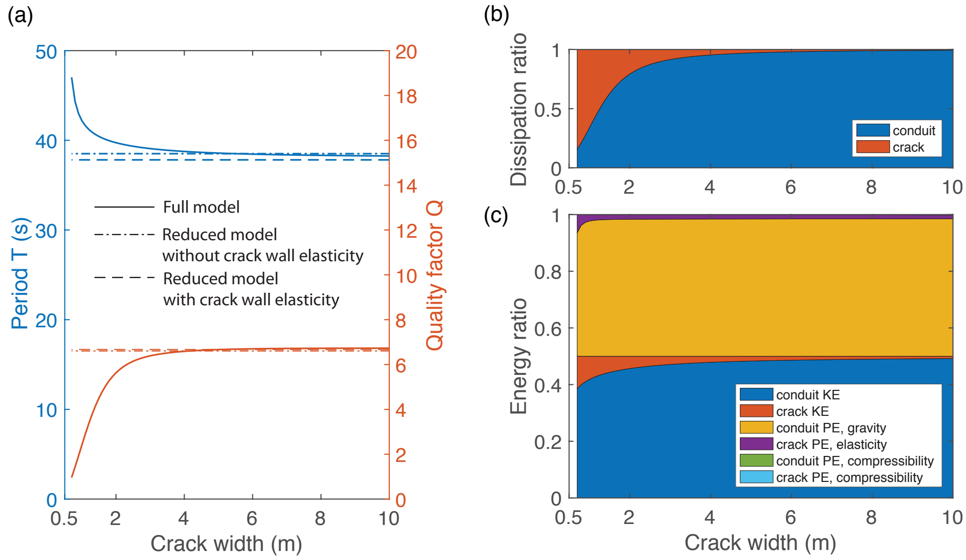

Figure B.6. Same as Figure B.1 but varying crack width.

Aster, R., S. Mah, P. Kyle, W. McIntosh, N. Dunbar, J. Johnson, M. Ruiz, and S. McNamara (2003), Very long period oscillations of Mount Erebus Volcano, *Journal of Geophysical Research: Solid Earth*, *108*(B11), doi:10.1029/2002JB002101.

Aster, R., D. Zandomeneghi, S. Mah, S. McNamara, D. Henderson, H. Knox, and K. Jones (2008), Moment tensor inversion of very long period seismic signals from Strombolian eruptions of Erebus Volcano, *Journal of Volcanology and Geothermal Research*, *177*(3), 635–647, doi:10.1016/j.jvolgeores.2008.08.013.

Carey, R. J., M. Manga, W. Degruyter, D. Swanson, B. Houghton, T. Orr, and M. Patrick (2012), Externally triggered renewed bubble nucleation in basaltic magma: The 12 October 2008 eruption at Halema‘uma ‘u Overlook vent, Kīlauea, Hawai‘i, USA, *Journal of Geophysical Research: Solid Earth*, *117*(B11), doi:10.1029/2012JB009496.

Carey, R. J., M. Manga, W. Degruyter, H. Gonnermann, D. Swanson, B. Houghton, T. Orr, and M. Patrick (2013), Convection in a volcanic conduit recorded by bubbles, *Geology*, *41*(4), 395–398, doi:10.1130/G33685.1.

Chouet, B. (1986), Dynamics of a fluid-driven crack in three dimensions by the finite difference method, *Journal of Geophysical Research: Solid Earth*, *91*(B14), 13,967–13,992, doi:10.1029/JB091iB14p13967.

Chouet, B., and P. Dawson (2011), Shallow conduit system at Kilauea Volcano, Hawaii, revealed by seismic signals associated with degassing bursts, *Journal of Geophysical Research: Solid Earth*, *116*(B12), doi:10.1029/2011JB008677.

Chouet, B., and P. Dawson (2013), Very long period conduit oscillations induced by rockfalls at Kilauea Volcano, Hawaii, *Journal of Geophysical Research: Solid Earth*, *118*(10), 5352–5371, doi:10.1002/jgrb.50376.

Chouet, B. A., P. B. Dawson, M. R. James, and S. J. Lane (2010), Seismic source mechanism of degassing bursts at Kilauea Volcano, Hawaii: Results from waveform inversion in the 10-50 s band, *Journal of Geophysical Research: Solid Earth*, *115*(B9), doi:10.1029/2009JB006661.

Crouch, S. L., A. M. Starfield, and F. Rizzo (1983), Boundary element methods in solid mechanics, *Journal of Applied Mechanics*, *50*, 704.

Dawson, P., and B. Chouet (2014), Characterization of very-long-period seismicity accompanying summit activity at Kilauea Volcano, Hawai‘i: 2007-2013, *Journal of Volcanology and Geothermal Research*, *278-279*, 59 – 85, doi:https://doi.org/10.1016/j.jvolgeores.

2014.04.010.

Dawson, P. B., M. C. Benítez, B. A. Chouet, D. Wilson, and P. G. Okubo (2010), Monitoring very-long-period seismicity at Kilauea Volcano, Hawaii, *Geophysical Research Letters*, *37*(18), doi:10.1029/2010GL044418.

Fee, D., M. Garcés, M. Patrick, B. Chouet, P. Dawson, and D. Swanson (2010), Infrasonic harmonic tremor and degassing bursts from Halema'uma'u Crater, Kilauea Volcano, Hawai'i, *Journal of Geophysical Research: Solid Earth*, *115*(B11), doi:10.1029/2010JB007642.

Ferrazzini, V., and K. Aki (1987), Slow waves trapped in a fluid-filled infinite crack: Implication for volcanic tremor, *Journal of Geophysical Research: Solid Earth*, *92*(B9), 9215–9223, doi:10.1029/JB092iB09p09215.

Fowler, A., and M. Robinson (2018), Counter-current convection in a volcanic conduit, *Journal of Volcanology and Geothermal Research*, *356*, 141–162, doi:10.1016/j.jvolgeores.2018.03.004.

Fujita, E., K. Araki, and K. Nagano (2011), Volcanic tremor induced by gas-liquid two-phase flow: Implications of density wave oscillation, *Journal of Geophysical Research: Solid Earth*, *116*(B9), doi:10.1029/2010JB008068.

Garces, M. (2000), Theory of acoustic propagation in a multi-phase stratified liquid flowing within an elastic-walled conduit of varying cross-sectional area, *Journal of volcanology and geothermal research*, *101*(1-2), 1–17, doi:10.1016/S0377-0273(00)00155-4.

Gill, A. E. (1982), *Atmosphere-Ocean Dynamics*, Academia Press, INC.

Green, E. I. (1955), The story of q, *American Scientist*, *43*(4), 584–594.

Hayek, S. I. (2003), Mechanical vibration and damping, *digital Encyclopedia of Applied Physics*.

Jaeger, J. C., N. G. Cook, and R. Zimmerman (2009), *Fundamentals of rock mechanics*, John Wiley & Sons.

James, M., S. Lane, B. Chouet, and J. Gilbert (2004), Pressure changes associated with the ascent and bursting of gas slugs in liquid-filled vertical and inclined conduits, *Journal of Volcanology and Geothermal Research*, *129*(1-3), 61–82, doi:10.1016/S0377-0273(03)00232-4.

Karlstrom, L., and E. M. Dunham (2016), Excitation and resonance of acoustic-gravity waves in a column of stratified, bubbly magma, *Journal of Fluid Mechanics*, *797*, 431–470, doi:10.1017/jfm.2016.257.

Knox, H., J. Chaput, R. Aster, and P. Kyle (2018), Multiyear shallow conduit changes observed with lava lake eruption seismograms at erebus volcano, antarctica, *Journal of Geophysical Research: Solid Earth*, *123*(4), 3178–3196, doi:10.1002/2017JB015045.

Korneev, V. (2008), Slow waves in fractures filled with viscous fluid, *Geophysics*, *73*(1), N1–N7, doi:10.1190/1.2802174.

Krauklis, P. V. (1962), On some low-frequency oscillations of a fluid layer in an elastic medium, *Prikl. Mat. Mekh.*, *26*(6), 1111–1115, doi:10.1016/0021-8928(63)90084-4.

Kreiss, H.-O., and G. Scherer (1974), Finite element and finite difference methods for hyperbolic partial differential equations, in *Mathematical aspects of finite elements in partial differential equations*, pp. 195–212, Elsevier.

Liang, C., O. O'Reilly, E. M. Dunham, and D. Moos (2017), Hydraulic fracture diagnostics from Krauklis-wave resonance and tube-wave reflections, *Geophysics*, *82*(3), D171–D186, doi:10.1190/geo2016-0480.1.

Lipovsky, B. P., and E. M. Dunham (2015), Vibrational modes of hydraulic fractures: Inference of fracture geometry from resonant frequencies and attenuation, *Journal of Geophysical Research: Solid Earth*, *120*(2), 1080–1107, doi:10.1002/2014JB011286.

Mah, S. (2003), Discrimination of Strombolian eruption types using very long period (VLP) seismic signals and video observations at Mount Erebus, Antarctica, *MS Independent Study, New Mexico Institute of Mining and Technology*.

McTigue, D. (1987), Elastic stress and deformation near a finite spherical magma body: resolution of the point source paradox, *Journal of Geophysical Research: Solid Earth*, *92*(B12), 12,931–12,940, doi:10.1029/JB092iB12p12931.

Mizuno, N., M. Ichihara, and N. Kame (2015), Moment tensors associated with the expansion and movement of fluid in ellipsoidal cavities, *Journal of Geophysical Research: Solid Earth*, *120*(9), 6058–6070, doi:10.1002/2015JB012084.

Mogi, K. (1958), Relations between the eruptions of various volcanoes and the deformations of the ground surfaces around them, *Bull. Earthquake Res Inst. Univ. Tokyo*, *36*, 99–134.

Ohminato, T., B. A. Chouet, P. Dawson, and S. Kedar (1998), Waveform inversion of very long period impulsive signals associated with magmatic injection beneath Kilauea Volcano, Hawaii, *Journal of Geophysical Research: Solid Earth*, *103*(B10), 23,839–23,862, doi:10.1029/98JB01122.

Okada, Y. (1985), Surface deformation due to shear and tensile faults in a half-space, *Bulletin of the seismological society of America*, *75*(4), 1135–1154.

Okada, Y. (1992), Internal deformation due to shear and tensile faults in a half-space, *Bulletin of the Seismological Society of America*, *82*(2), 1018–1040.

Olsson, P. (1995), Summation by parts, projections, and stability. I, *Mathematics of Computation*, *64*(211), 1035–1065, doi:10.1090/S0025-5718-1995-1297474-X.

O'Reilly, O., E. M. Dunham, and J. Nordström (2017), Simulation of wave propagation along fluid-filled cracks using high-order summation-by-parts operators and implicit-explicit time stepping, *SIAM Journal on Scientific Computing*, *39*(4), B675–B702, doi:10.1137/16M1097511.

Orr, T. R., W. A. Thelen, M. R. Patrick, D. A. Swanson, and D. C. Wilson (2013), Explosive eruptions triggered by rockfalls at Kīlauea volcano, Hawai'i, *Geology*, *41*(2), 207–210, doi:10.1130/G33564.1.

Patrick, M., D. Wilson, D. Fee, T. Orr, and D. Swanson (2011), Shallow degassing events as a trigger for very-long-period seismicity at Kīlauea Volcano, Hawai'i, *Bulletin of Volcanology*, *73*(9), 1179–1186, doi:10.1007/s00445-011-0475-y.

Patrick, M. R., T. R. Orr, A. J. Sutton, T. Elias, and D. A. Swanson (2013), The first five years of Kīlauea's summit eruption in Halema'uma'u Crater, 2008–2013: U.s. geological survey fact sheet 2013-3116, 4 p, *Tech. rep.*, US Geological Survey, doi:10.3133/fs20133116.

Prochnow, B., O. O'Reilly, E. M. Dunham, and N. A. Petersson (2017), Treatment of the polar coordinate singularity in axisymmetric wave propagation using high-order summation-by-parts operators on a staggered grid, *Computers & Fluids*, *149*, 138–149, doi:10.1016/j.compfluid.2017.03.015.

Rivalta, E., and P. Segall (2008), Magma compressibility and the missing source for some dike intrusions, *Geophysical Research Letters*, *35*(4), doi:10.1029/2007GL032521.

Rowe, C., R. Aster, P. Kyle, R. Dibble, and J. Schlue (2000), Seismic and acoustic observations at Mount Erebus volcano, Ross island, Antarctica, 1994-1998, *Journal of Volcanology and Geothermal Research*, *101*(1-2), 105–128, doi:10.1016/S0377-0273(00)00170-0.

Sneddon, I. N. (1946), The distribution of stress in the neighbourhood of a crack in an elastic solid, *Proceedings of the Royal Society of London. Series A. Mathematical and Physical Sciences*, *187*(1009), 229–260, doi:10.1098/rspa.1946.0077.

Staecker, P., and W. Wang (1973), Propagation of elastic waves bound to a fluid layer between two solids, *The Journal of the Acoustical Society of America*, *53*(1), 65–74, doi:10.1121/1.1913329.

Strand, B. (1994), Summation by parts for finite difference approximations for d/dx, *Journal of Computational Physics*, *110*(1), 47 – 67, doi:https://doi.org/10.1006/jcph.1994.1005.

Waite, G. P. (2014), *Very-Long-Period Seismicity at Active Volcanoes: Source Mechanisms*, pp. 1–12, Springer Berlin Heidelberg, Berlin, Heidelberg, doi:10.1007/978-3-642-36197-5_46-1.

schematics.

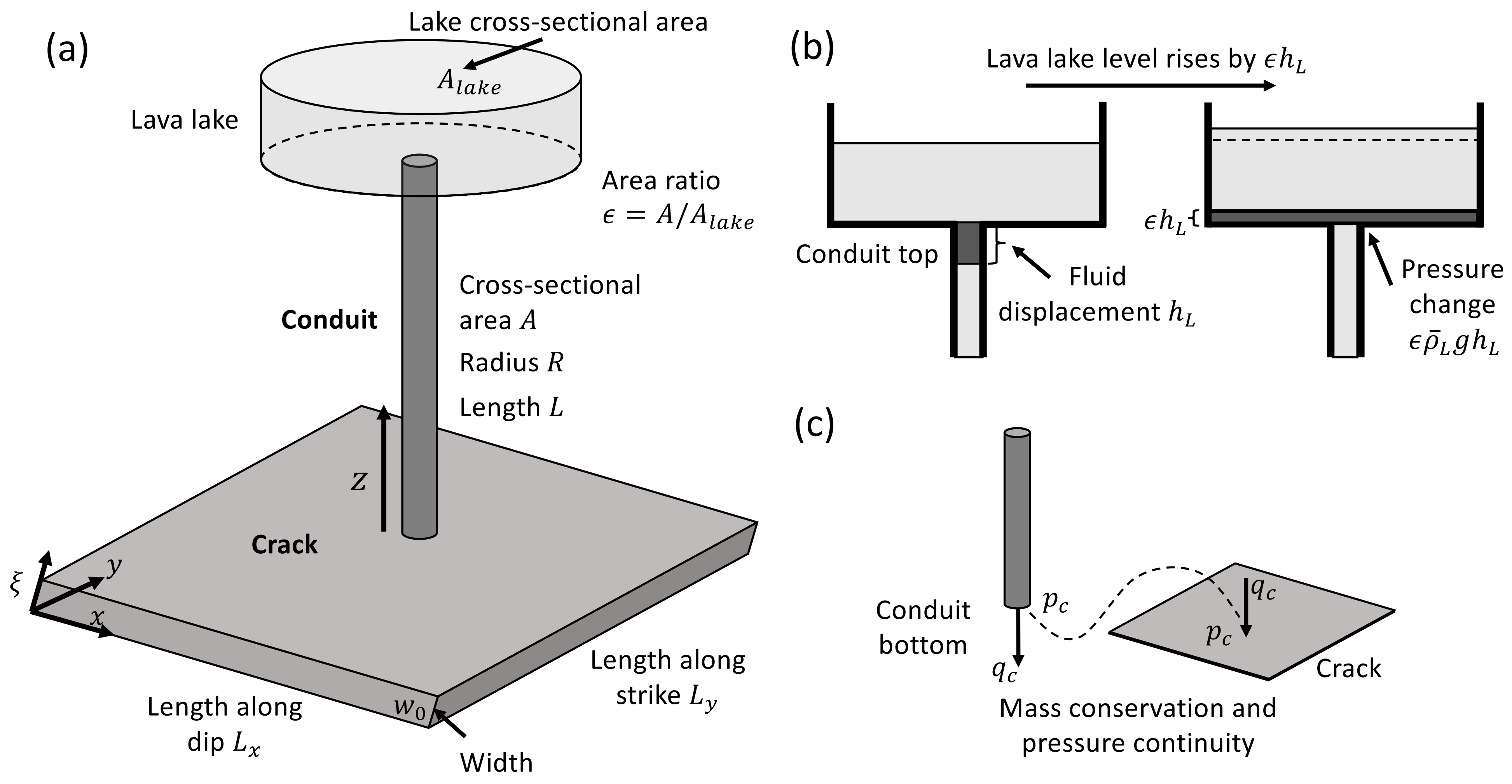
(a)
Lake cross-sectional area
A_{lake}
Lava lake
Area ratio
$\epsilon = A/A_{lake}$
Cross-sectional area A
Conduit
Radius R
Length L
z
Crack
ξ
y
x
Length along strike L_y
Length along dip L_x
w_0
Width
(b)
Lava lake level rises by ϵh_L
Conduit top
Fluid displacement h_L
ϵh_L
Pressure change
$\epsilon \bar{\rho}_L g h_L$
(c)
Conduit bottom
p_c
q_c
q_c
p_c
Crack
Mass conservation and pressure continuity

space_time_plots.

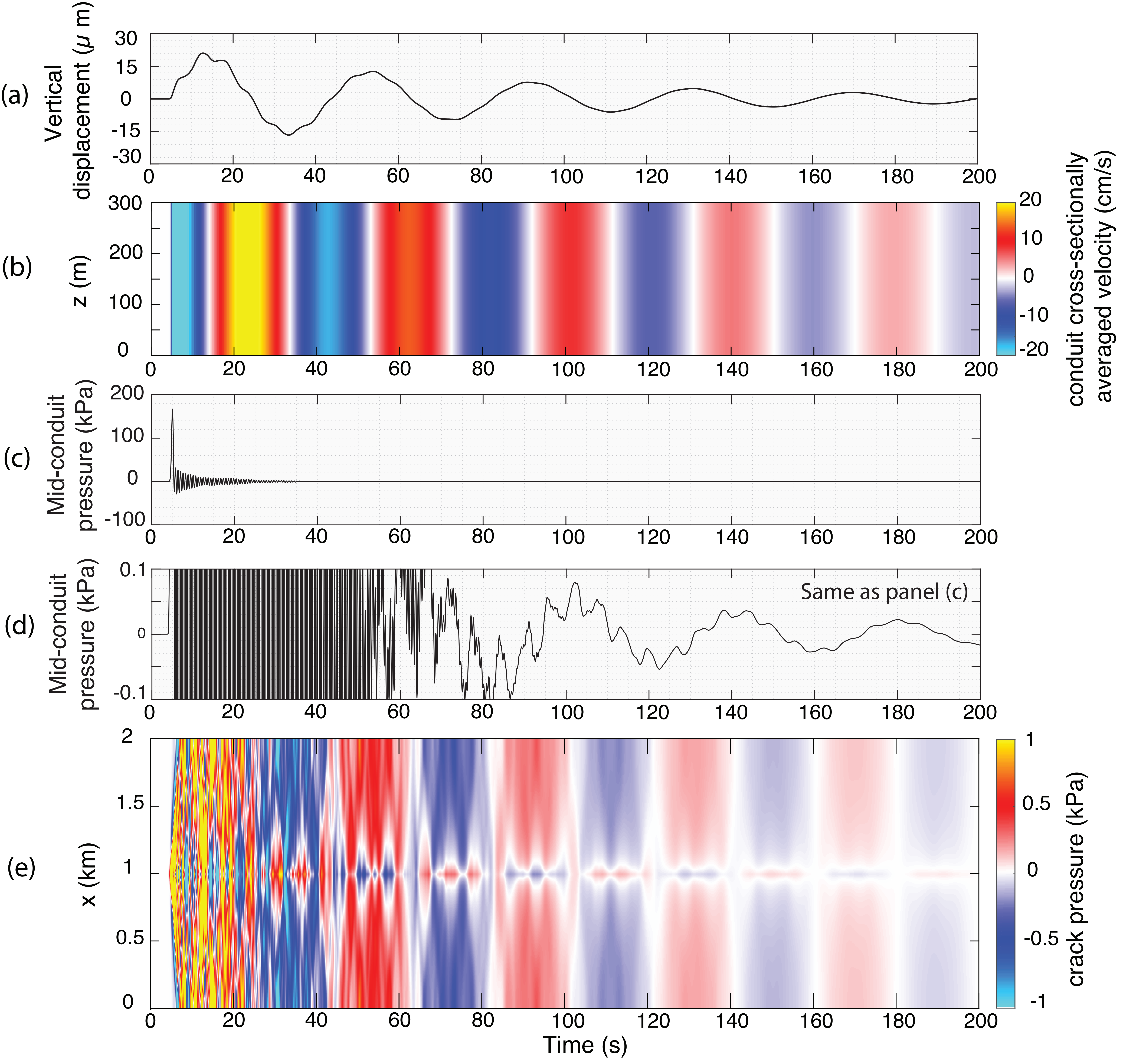
(a)
Vertical displacement (μ m)
30
15
0
-15
-30
0 20 40 60 80 100 120 140 160 180 200
(b)
z (m)
300
200
100
0
conduit cross-sectionally averaged velocity (cm/s)
20
10
0
-10
-20
(c)
Mid-conduit pressure (kPa)
200
100
0
-100
(d)
Mid-conduit pressure (kPa)
0.1
0
-0.1
Same as panel (c)
(e)
x (km)
2
1.5
1
0.5
0
crack pressure (kPa)
1
0.5
0
-0.5
-1
Time (s)

snapshots.

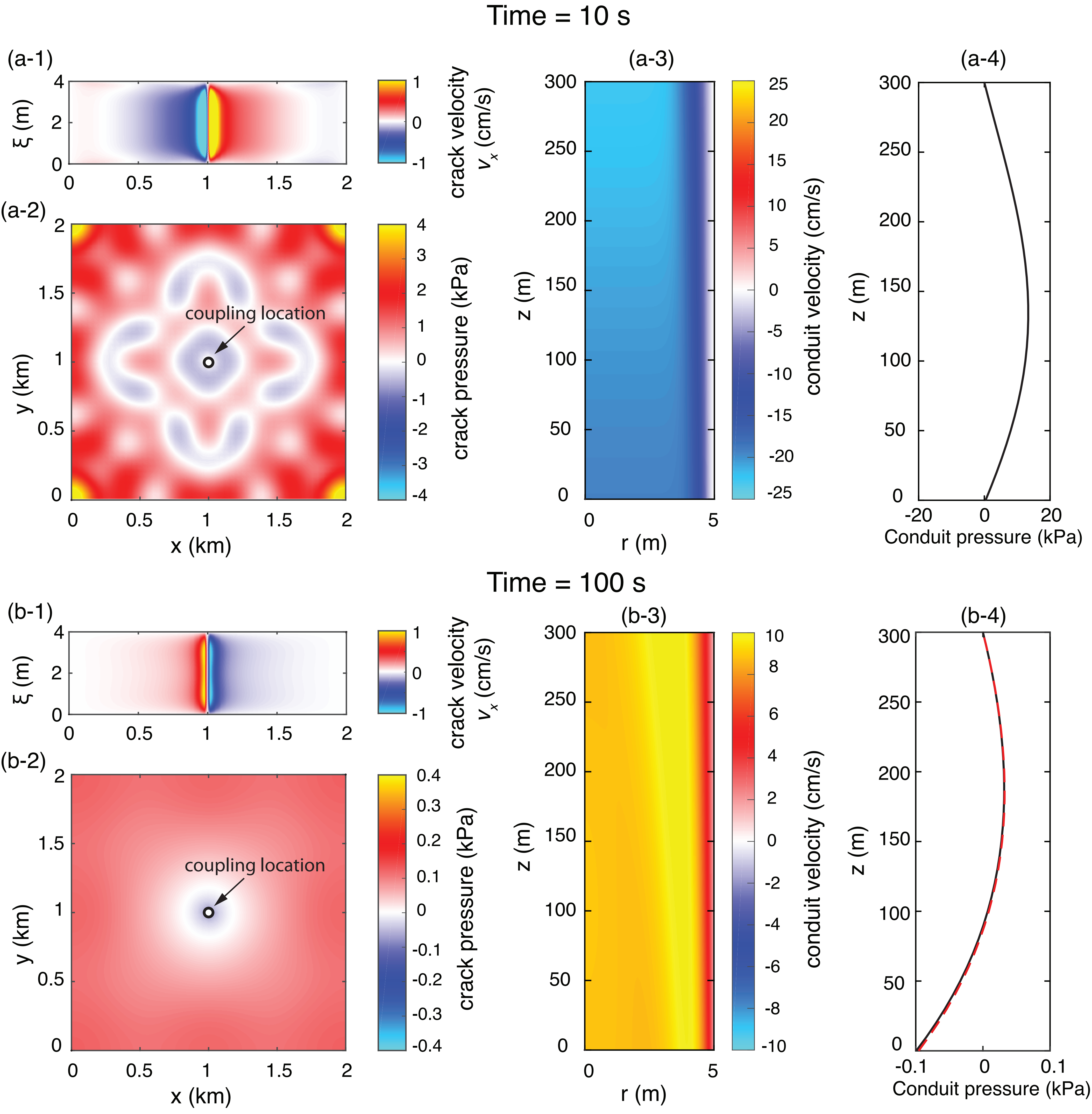

Time = 10 s
(a-1)
ξ (m)
crack velocity v_x (cm/s)
(a-2)
coupling location
y (km)
x (km)
crack pressure (kPa)
(a-3)
z (m)
r (m)
conduit velocity (cm/s)
(a-4)
z (m)
Conduit pressure (kPa)
Time = 100 s
(b-1)
ξ (m)
crack velocity v_x (cm/s)
(b-2)
coupling location
y (km)
x (km)
crack pressure (kPa)
(b-3)
z (m)
r (m)
conduit velocity (cm/s)
(b-4)
z (m)
Conduit pressure (kPa)

us_spectrum.

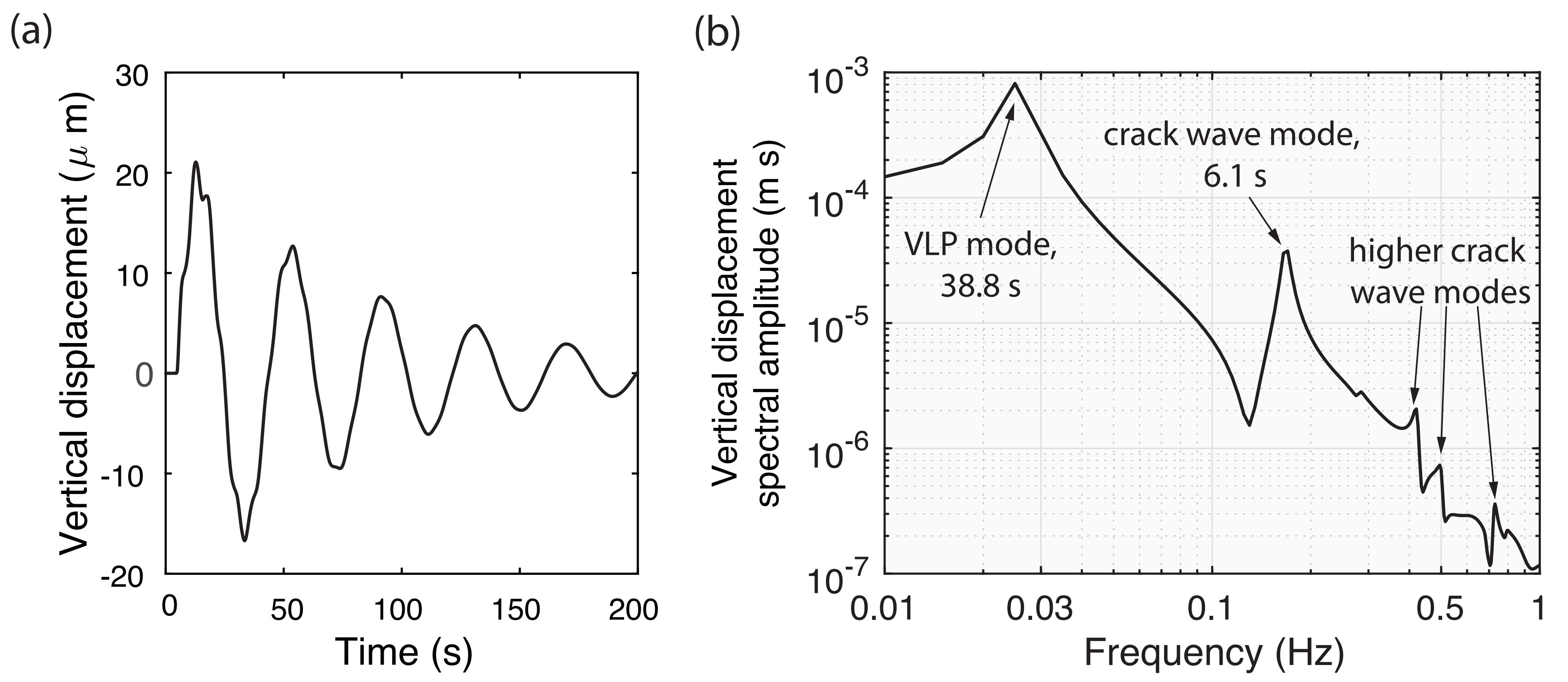

(a)
(b)
30
20
10
0
-10
-20
0
50
100
150
200
Time (s)
Vertical displacement (μ m)
10^{-3}
10^{-4}
10^{-5}
10^{-6}
10^{-7}
0.01
0.03
0.1
0.5
1
Frequency (Hz)
Vertical displacement spectral amplitude (m s)
VLP mode, 38.8 s
crack wave mode, 6.1 s
higher crack wave modes

mode_vlp.

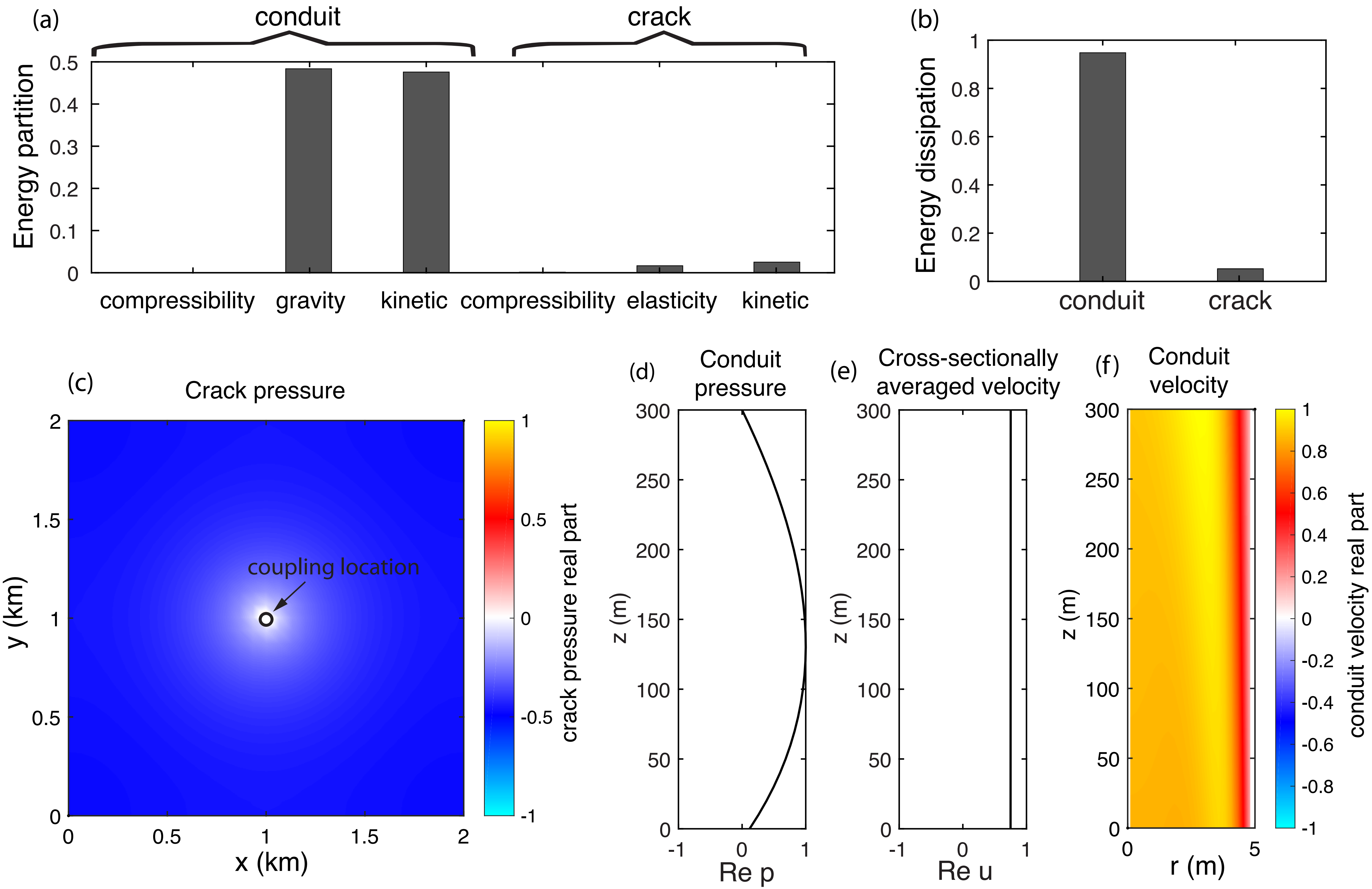
(a)
conduit
crack
Energy partition
0.5
0.4
0.3
0.2
0.1
0
compressibility
gravity
kinetic
compressibility
elasticity
kinetic
(b)
Energy dissipation
1
0.8
0.6
0.4
0.2
0
conduit
crack
(c)
Crack pressure
coupling location
y (km)
x (km)
crack pressure real part
(d)
Conduit pressure
z (m)
Re p
(e)
Cross-sectionally averaged velocity
z (m)
Re u
(f)
Conduit velocity
z (m)
r (m)
conduit velocity real part

mode_vlp_disp.

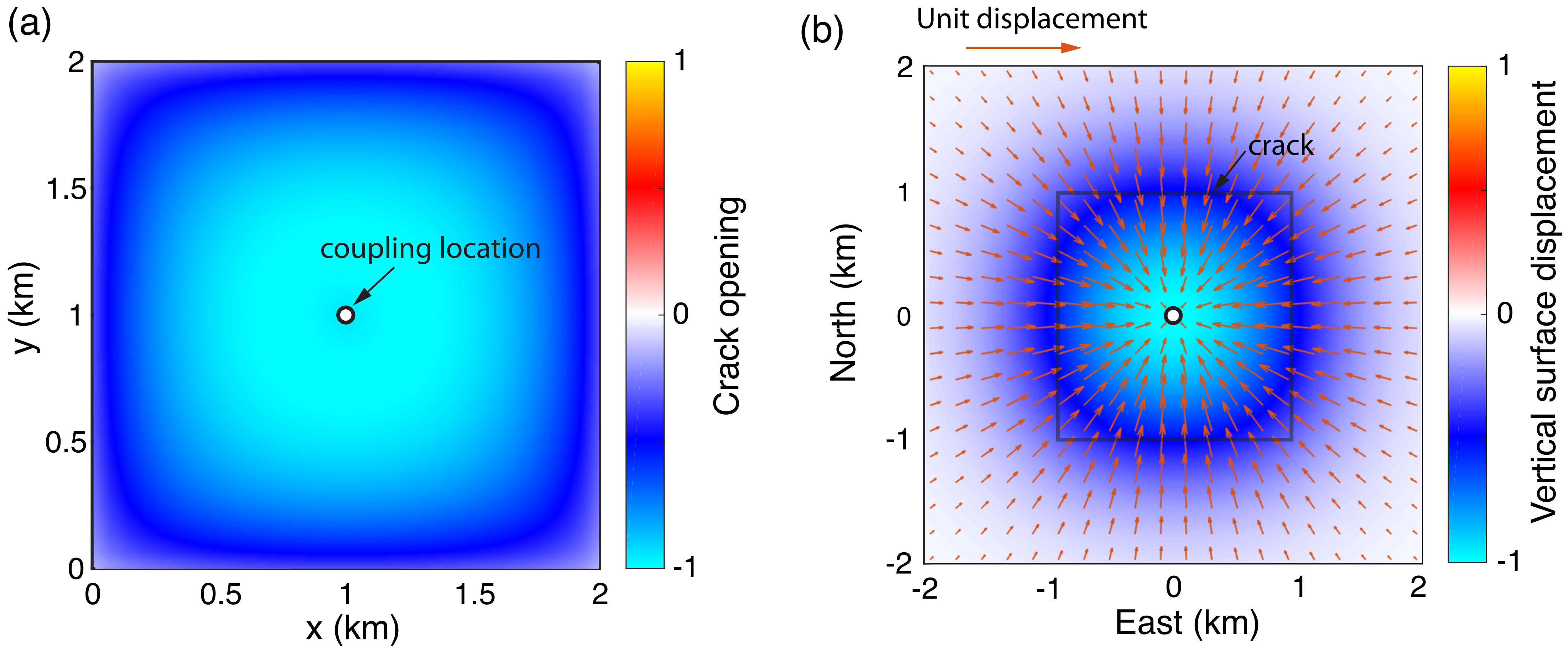

(a)
coupling location
Crack opening
y (km)
x (km)
2
1.5
1
0.5
0
0
0.5
1
1.5
2
1
0
-1
(b)
Unit displacement
crack
North (km)
East (km)
Vertical surface displacement
2
1
0
-1
-2
-2
-1
0
1
2
1
0
-1

mode_crack_1.

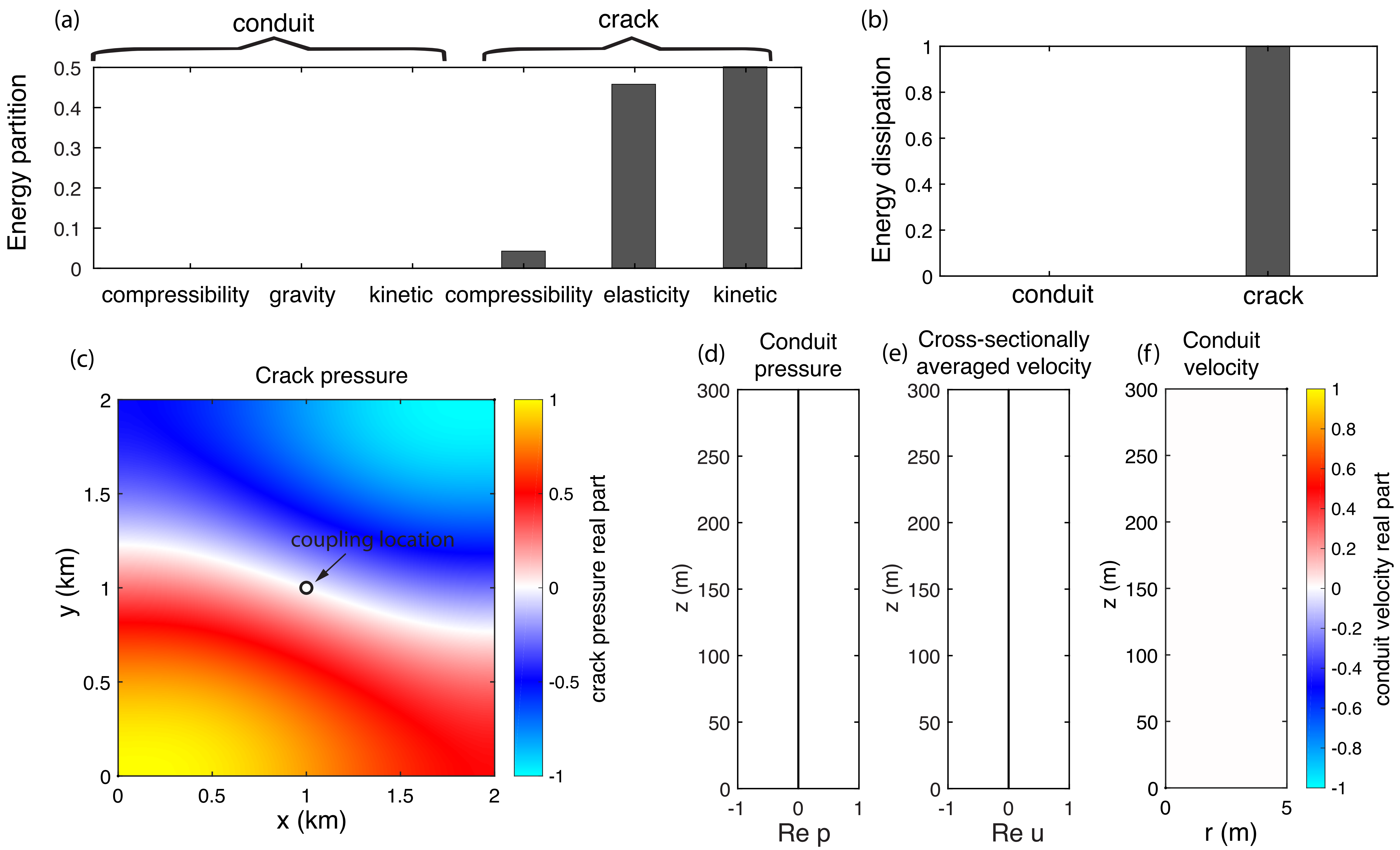
(a)
conduit
crack
Energy partition
0.5
0.4
0.3
0.2
0.1
0
compressibility
gravity
kinetic
compressibility
elasticity
kinetic
(b)
Energy dissipation
1
0.8
0.6
0.4
0.2
0
conduit
crack
(c)
Crack pressure
coupling location
y (km)
x (km)
crack pressure real part
(d)
Conduit pressure
z (m)
Re p
(e)
Cross-sectionally averaged velocity
z (m)
Re u
(f)
Conduit velocity
z (m)
r (m)
conduit velocity real part

mode_crack_1_disp.

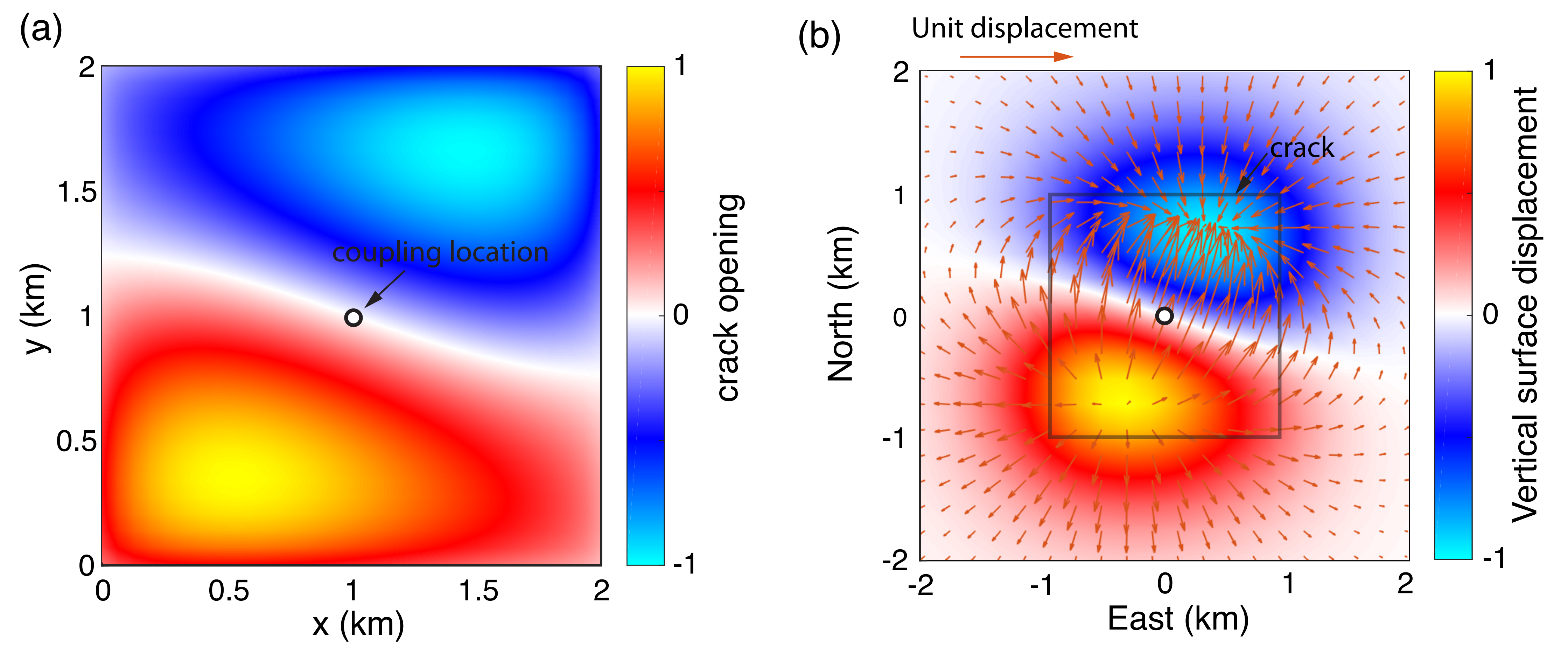
(a)
coupling location
crack opening
y (km)
x (km)
(b)
Unit displacement
crack
North (km)
East (km)
Vertical surface displacement

mode_crack_2.

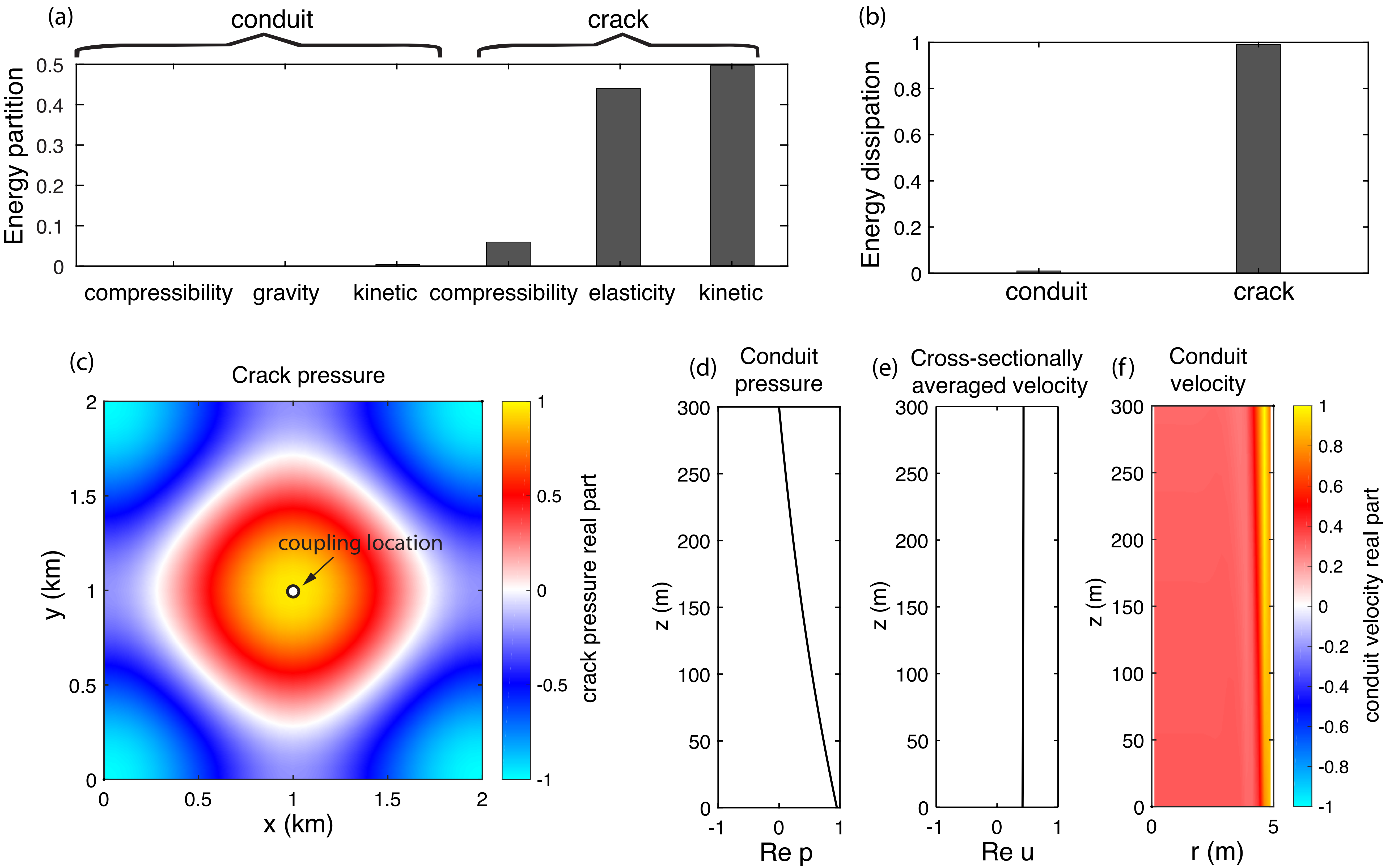

(a)
conduit
crack
Energy partition
0.5
0.4
0.3
0.2
0.1
0
compressibility
gravity
kinetic
compressibility
elasticity
kinetic
(b)
Energy dissipation
1
0.8
0.6
0.4
0.2
0
conduit
crack
(c)
Crack pressure
coupling location
y (km)
x (km)
crack pressure real part
(d)
Conduit pressure
z (m)
Re p
(e)
Cross-sectionally averaged velocity
z (m)
Re u
(f)
Conduit velocity
z (m)
r (m)
conduit velocity real part

mode_crack_2_disp.

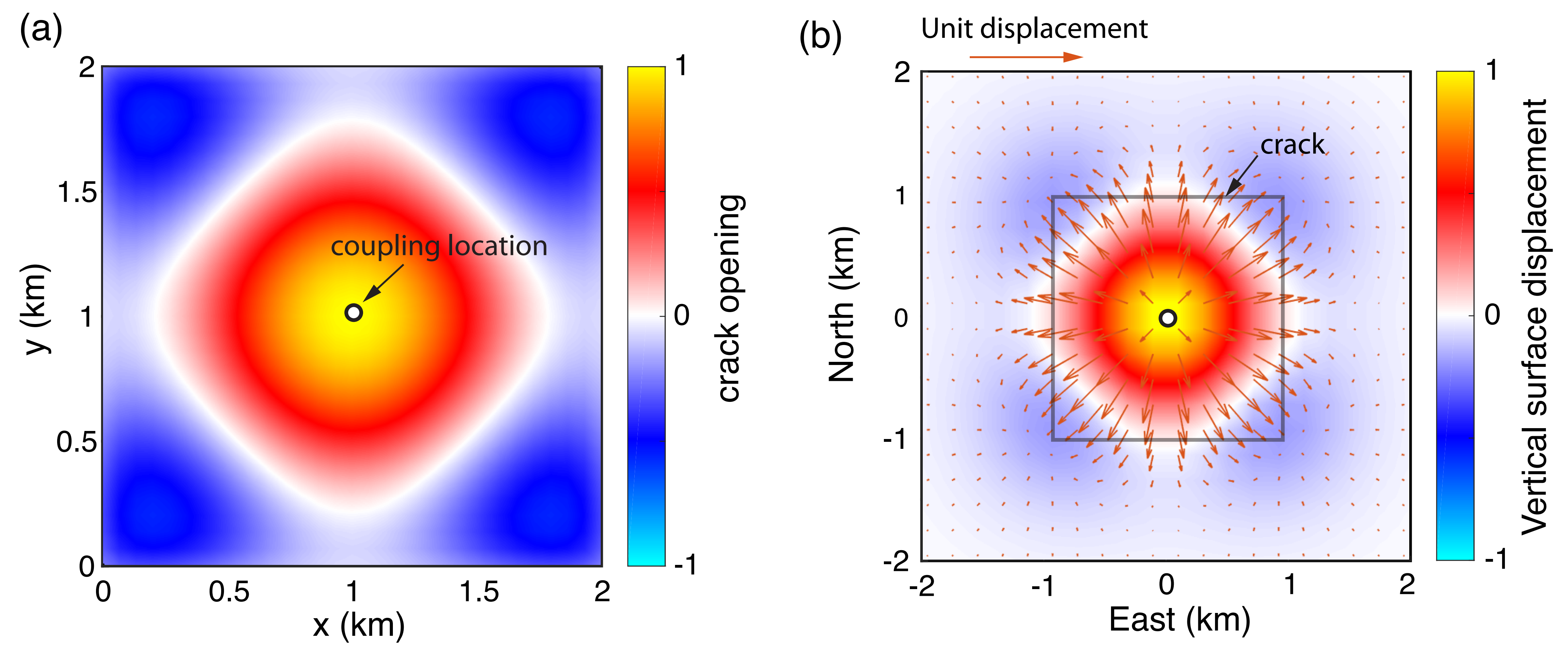

(a)
coupling location
y (km)
x (km)
crack opening
(b)
Unit displacement
crack
North (km)
East (km)
Vertical surface displacement

gravity_elasticity.

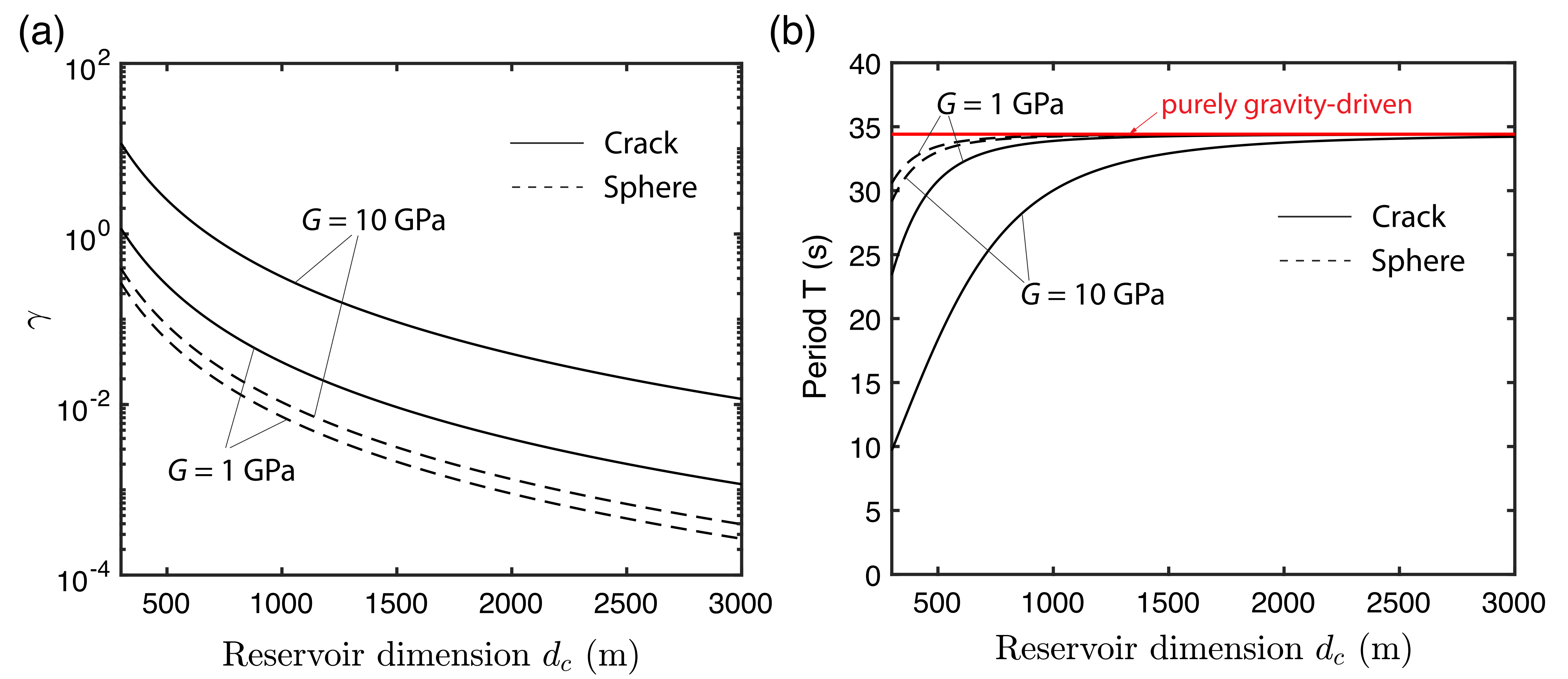

(a)
10^{2}
10^{0}
10^{-2}
10^{-4}
γ
Crack
Sphere
G = 10 GPa
G = 1 GPa
500
1000
1500
2000
2500
3000
Reservoir dimension d_c (m)
(b)
40
35
30
25
20
15
10
5
0
Period T (s)
G = 1 GPa
purely gravity-driven
Crack
Sphere
G = 10 GPa
500
1000
1500
2000
2500
3000
Reservoir dimension d_c (m)

TQv_nondimensional.

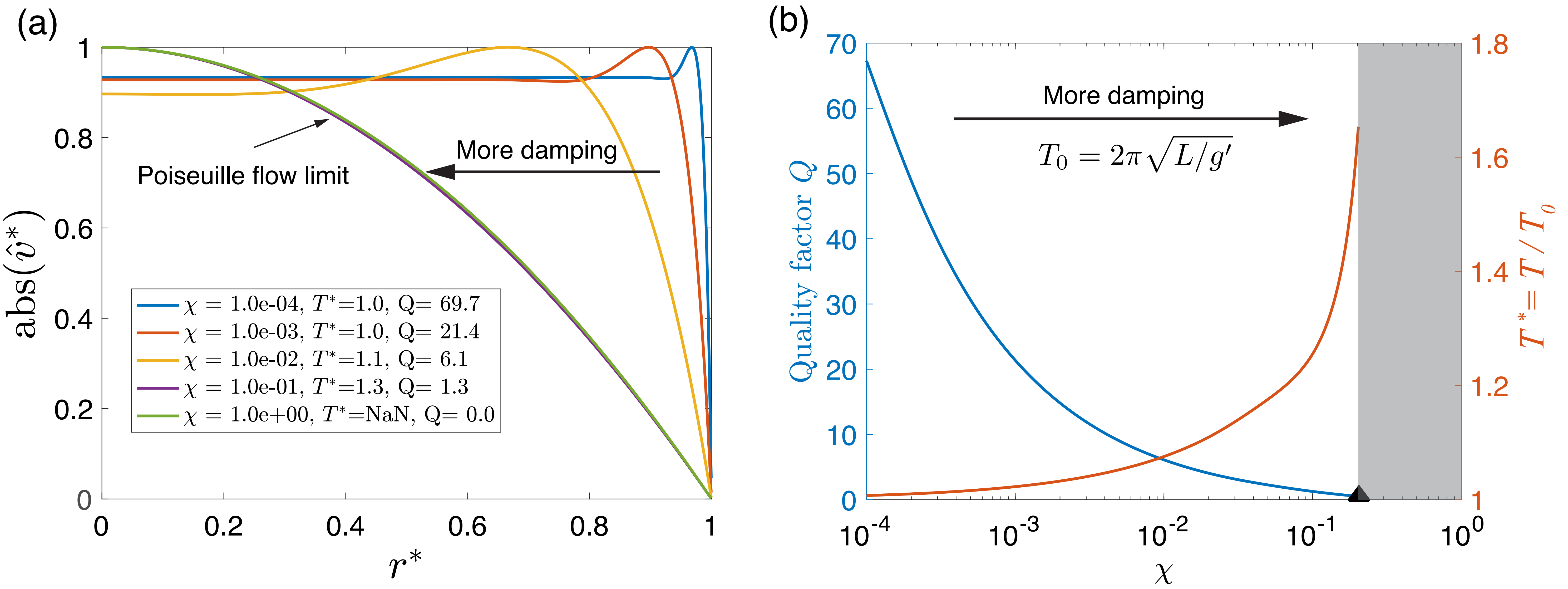
(a)
(b)
abs($\hat{v}^*$)
r^*
Poiseuille flow limit
More damping
χ = 1.0e-04, T^*=1.0, Q= 69.7
χ = 1.0e-03, T^*=1.0, Q= 21.4
χ = 1.0e-02, T^*=1.1, Q= 6.1
χ = 1.0e-01, T^*=1.3, Q= 1.3
χ = 1.0e+00, T^*=NaN, Q= 0.0
More damping
$T_0 = 2\pi\sqrt{L/g'}$
Quality factor Q
$T^* = T/T_0$
χ

h_amplify.

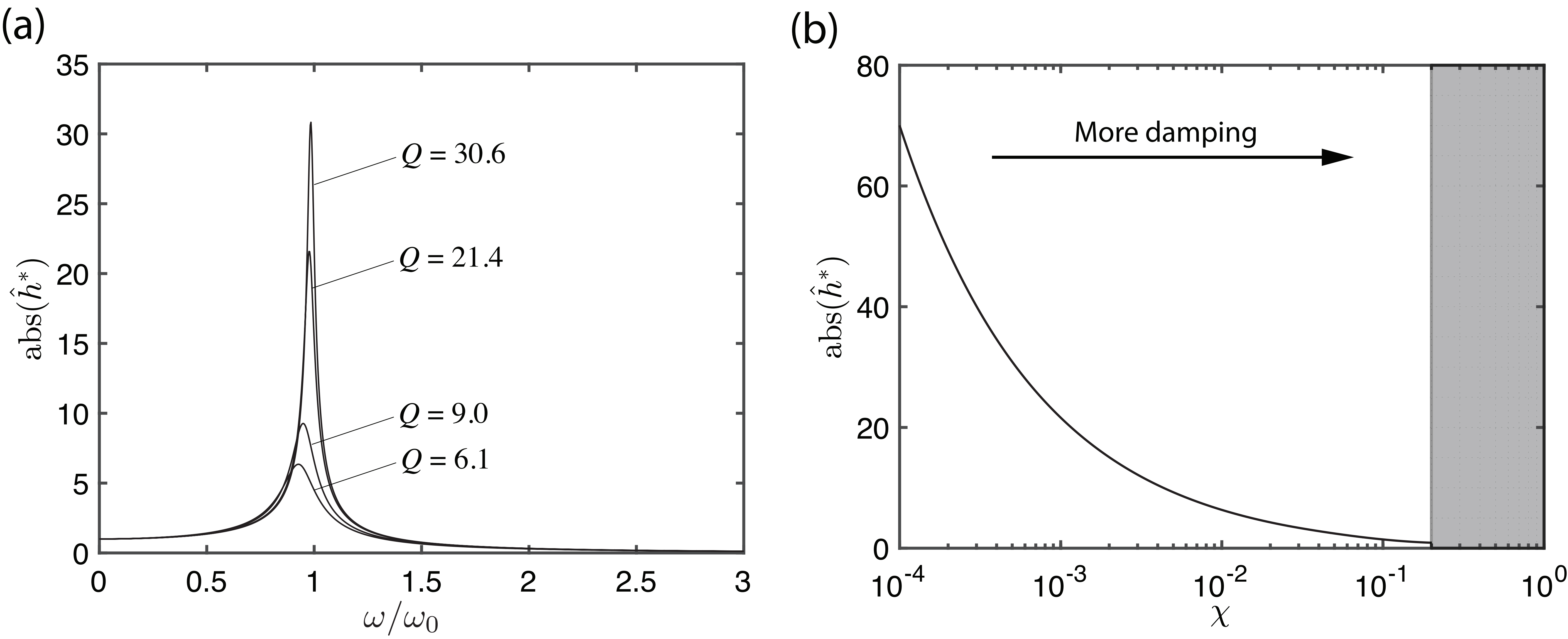

(a)
35
30
25
20
15
10
5
0
0
0.5
1
1.5
2
2.5
3
$\mathrm{abs}(\hat{h}^*)$
ω/ω_0
$Q = 30.6$
$Q = 21.4$
$Q = 9.0$
$Q = 6.1$
(b)
80
60
40
20
0
10^{-4}
10^{-3}
10^{-2}
10^{-1}
10^{0}
$\mathrm{abs}(\hat{h}^*)$
χ
More damping

nuR_muQ_T0.

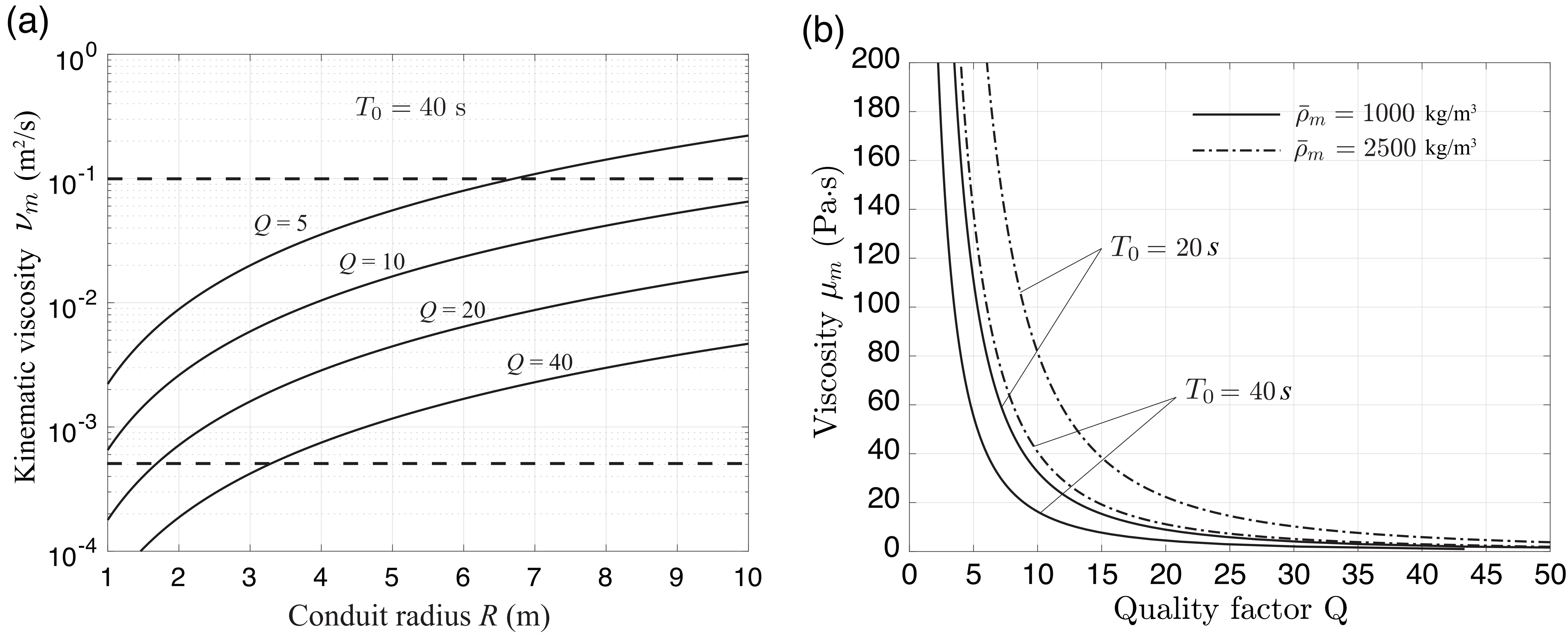
(a)
$T_0 = 40$ s
$Q = 5$
$Q = 10$
$Q = 20$
$Q = 40$
Kinematic viscosity ν_m (m²/s)
Conduit radius R (m)
(b)
$\bar{\rho}_m = 1000$ kg/m³
$\bar{\rho}_m = 2500$ kg/m³
$T_0 = 20\,s$
$T_0 = 40\,s$
Viscosity μ_m (Pa·s)
Quality factor Q

L_R_drho_tradeoffs.

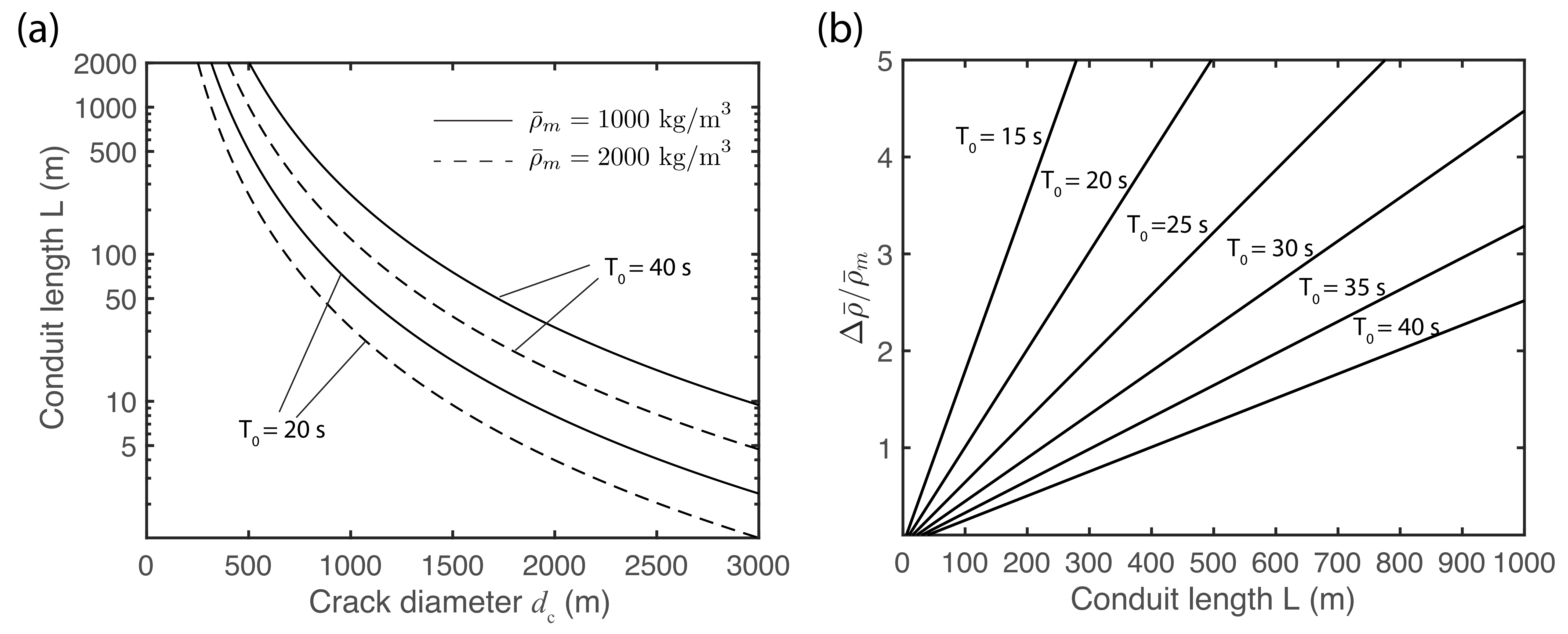

(a)
Conduit length L (m)
Crack diameter d_c (m)
$\bar{\rho}_m = 1000\ \mathrm{kg/m^3}$
$\bar{\rho}_m = 2000\ \mathrm{kg/m^3}$
$T_0 = 40$ s
$T_0 = 20$ s
2000
1000
500
100
50
10
5
0
500
1000
1500
2000
2500
3000
(b)
$\Delta\bar{\rho}/\bar{\rho}_m$
Conduit length L (m)
$T_0 = 15$ s
$T_0 = 20$ s
$T_0 = 25$ s
$T_0 = 30$ s
$T_0 = 35$ s
$T_0 = 40$ s
1
2
3
4
5
0
100
200
300
400
500
600
700
800
900
1000

para_Ls.

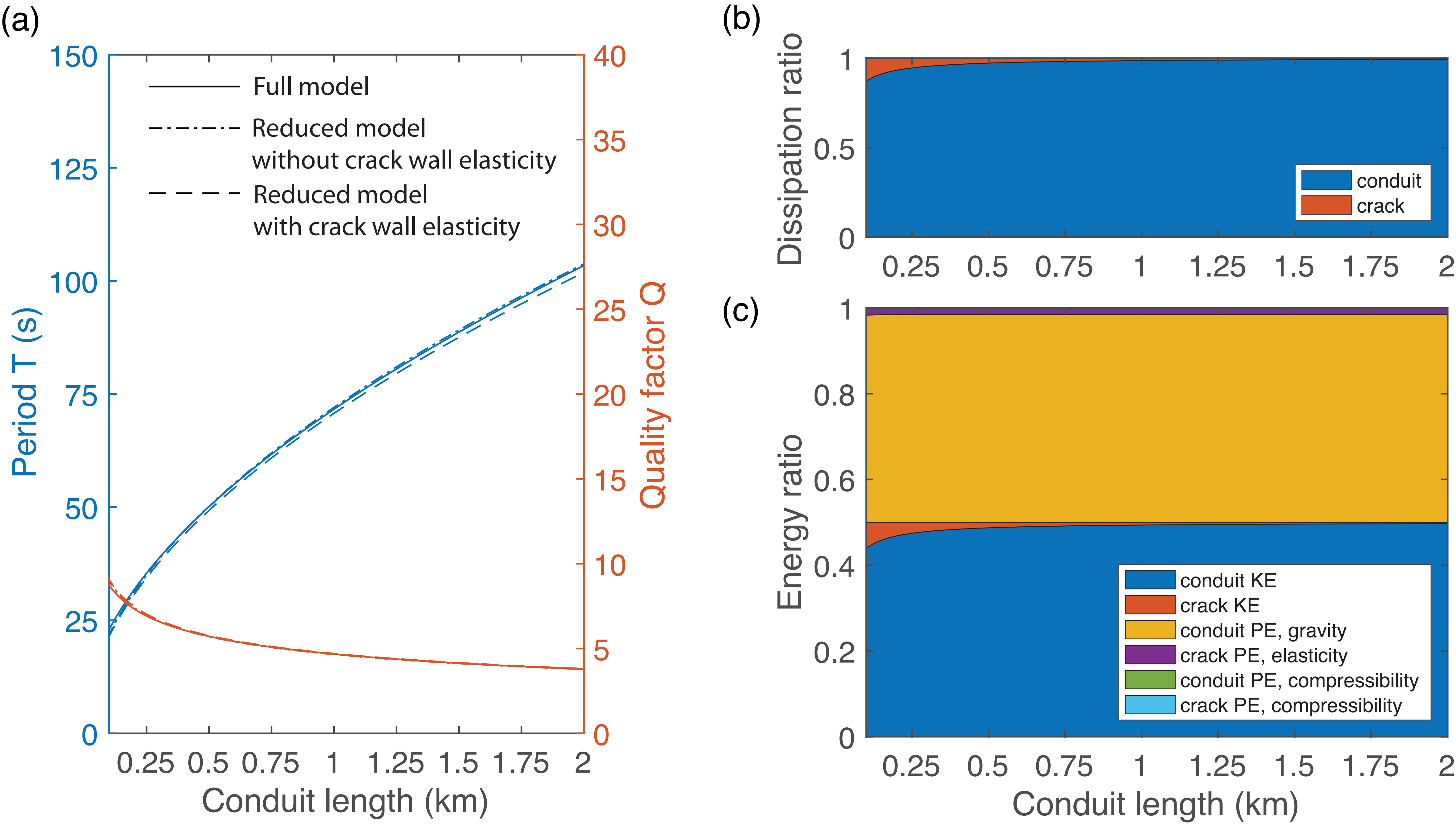

(a)
Full model
Reduced model
without crack wall elasticity
Reduced model
with crack wall elasticity
Period T (s)
Quality factor Q
Conduit length (km)
0
25
50
75
100
125
150
0
5
10
15
20
25
30
35
40
0.25
0.5
0.75
1
1.25
1.5
1.75
2
(b)
Dissipation ratio
conduit
crack
0
0.5
1
(c)
Energy ratio
conduit KE
crack KE
conduit PE, gravity
crack PE, elasticity
conduit PE, compressibility
crack PE, compressibility
0
0.2
0.4
0.6
0.8
1
Conduit length (km)

para_drhos.

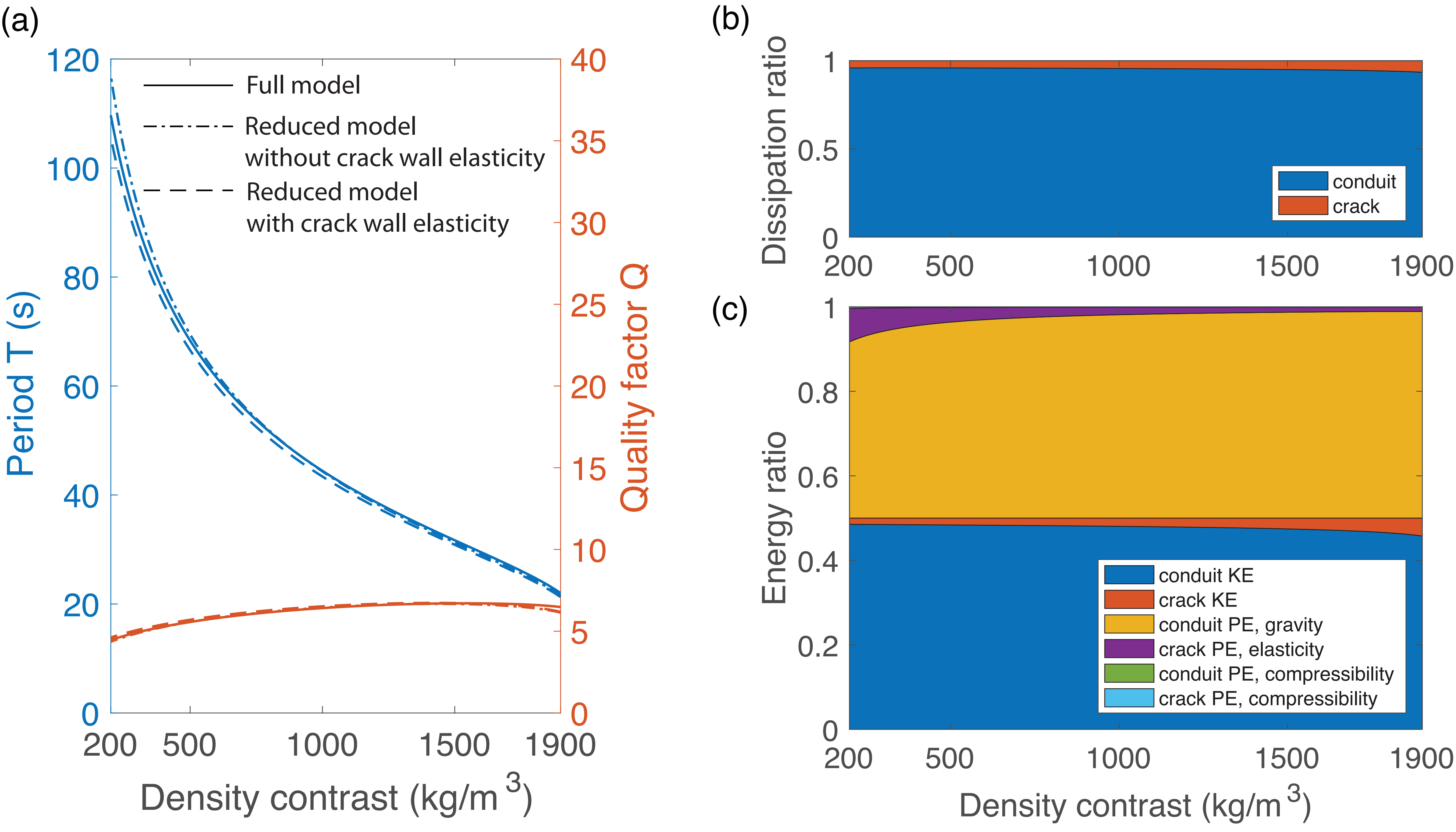

(a)
Full model
Reduced model without crack wall elasticity
Reduced model with crack wall elasticity
Period T (s)
Quality factor Q
Density contrast (kg/m 3)
(b)
Dissipation ratio
conduit
crack
(c)
Energy ratio
conduit KE
crack KE
conduit PE, gravity
crack PE, elasticity
conduit PE, compressibility
crack PE, compressibility
Density contrast (kg/m 3)

para_Lxys.

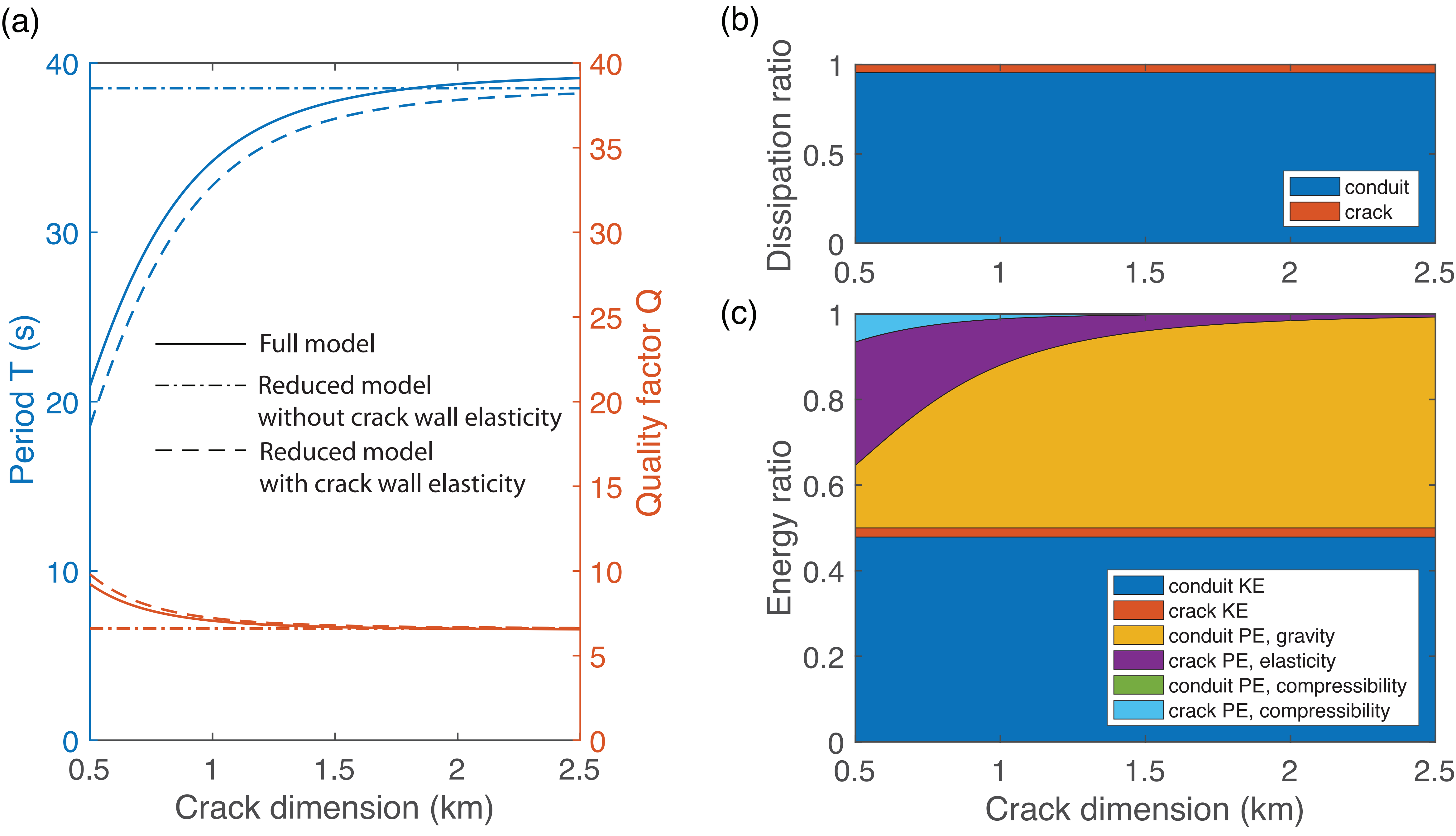

(a)
Period T (s)
Quality factor Q
Full model
Reduced model
without crack wall elasticity
Reduced model
with crack wall elasticity
Crack dimension (km)
(b)
Dissipation ratio
conduit
crack
(c)
Energy ratio
conduit KE
crack KE
conduit PE, gravity
crack PE, elasticity
conduit PE, compressibility
crack PE, compressibility
Crack dimension (km)

para_mus.

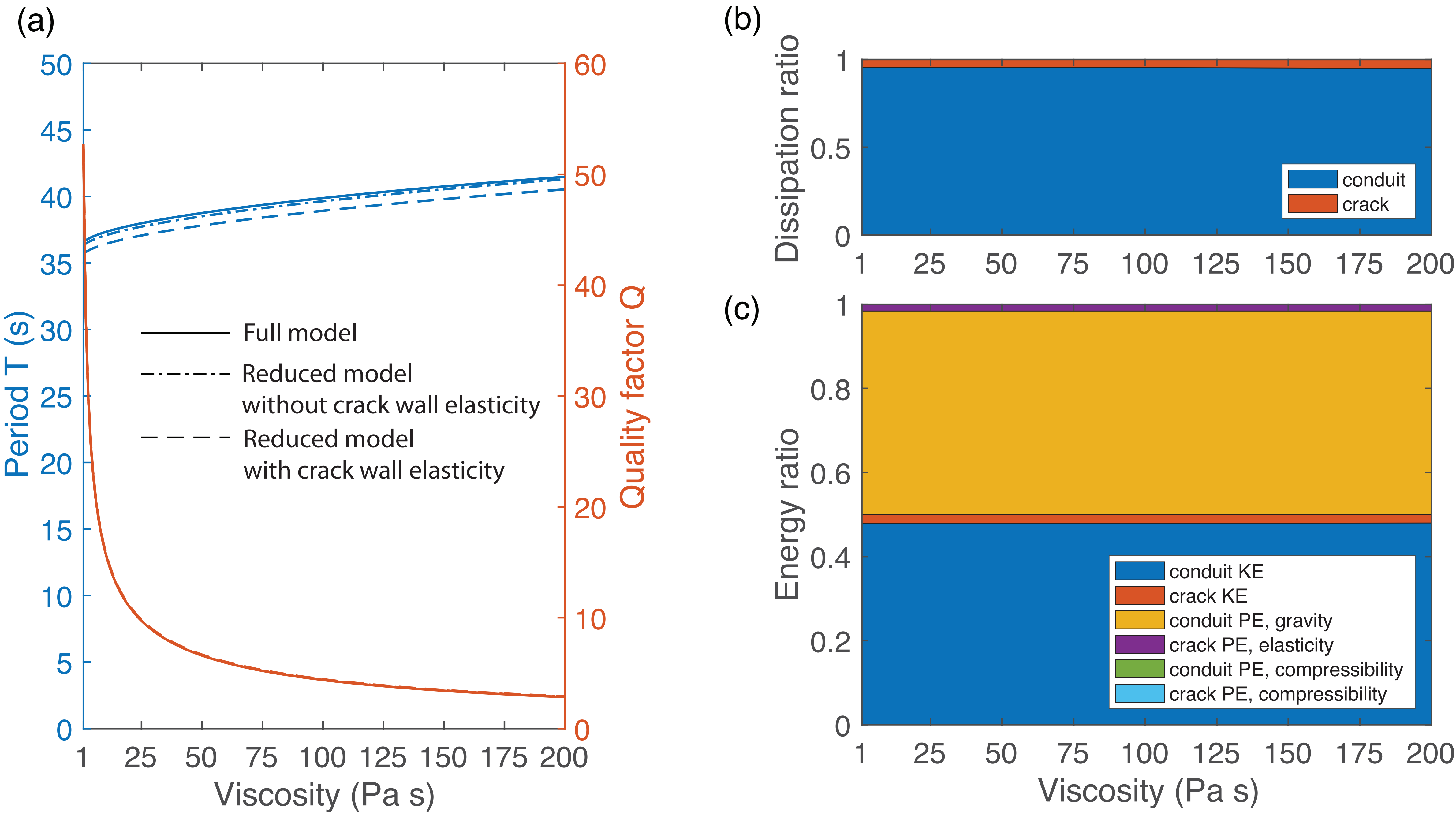
(a)
Period T (s)
Quality factor Q
Viscosity (Pa s)
Full model
Reduced model
without crack wall elasticity
Reduced model
with crack wall elasticity
(b)
Dissipation ratio
conduit
crack
(c)
Energy ratio
Viscosity (Pa s)
conduit KE
crack KE
conduit PE, gravity
crack PE, elasticity
conduit PE, compressibility
crack PE, compressibility

para_Rs.

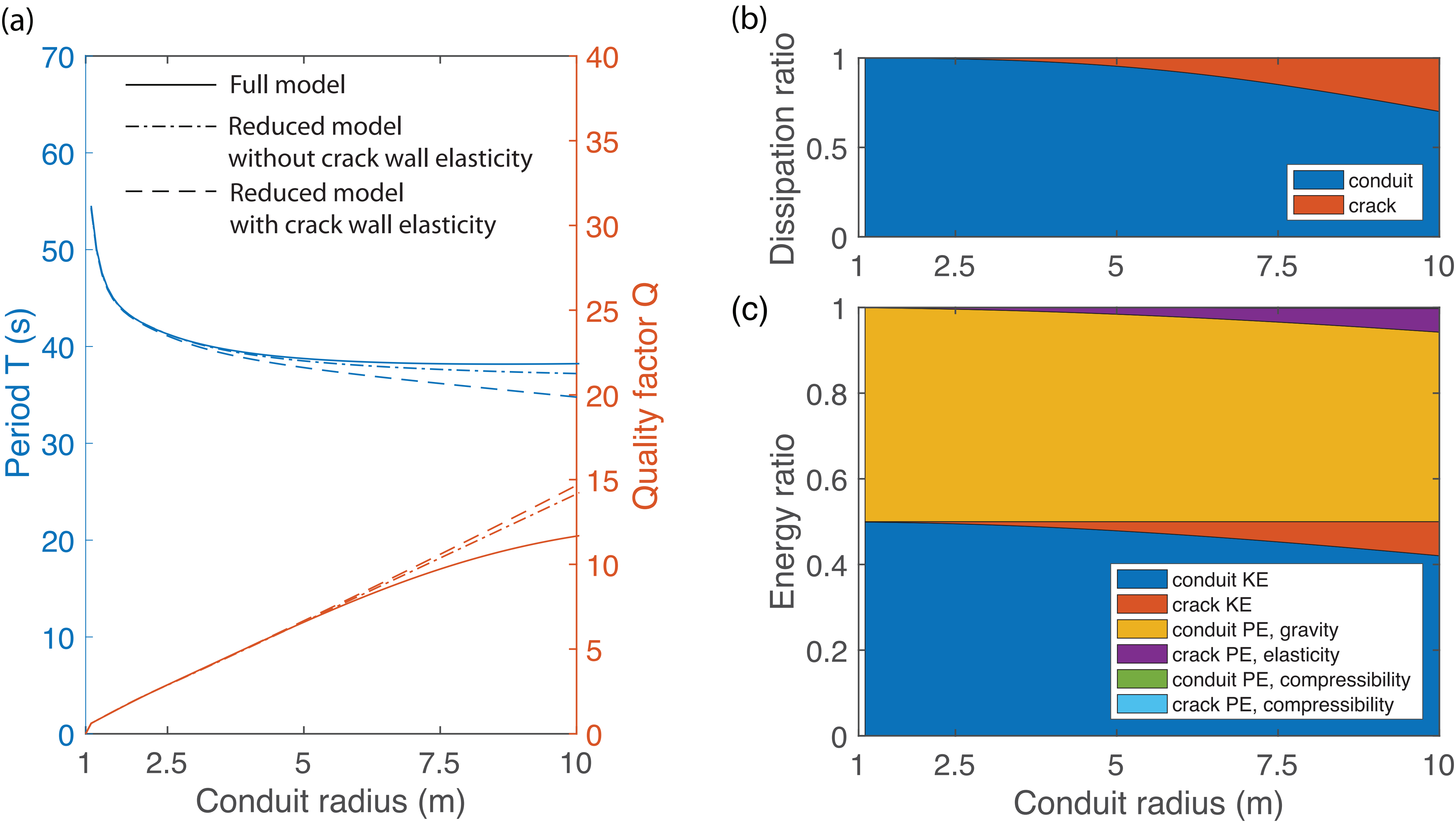
(a)
Full model
Reduced model
without crack wall elasticity
Reduced model
with crack wall elasticity
Period T (s)
Quality factor Q
Conduit radius (m)
(b)
Dissipation ratio
conduit
crack
(c)
Energy ratio
conduit KE
crack KE
conduit PE, gravity
crack PE, elasticity
conduit PE, compressibility
crack PE, compressibility
Conduit radius (m)

para_ws.

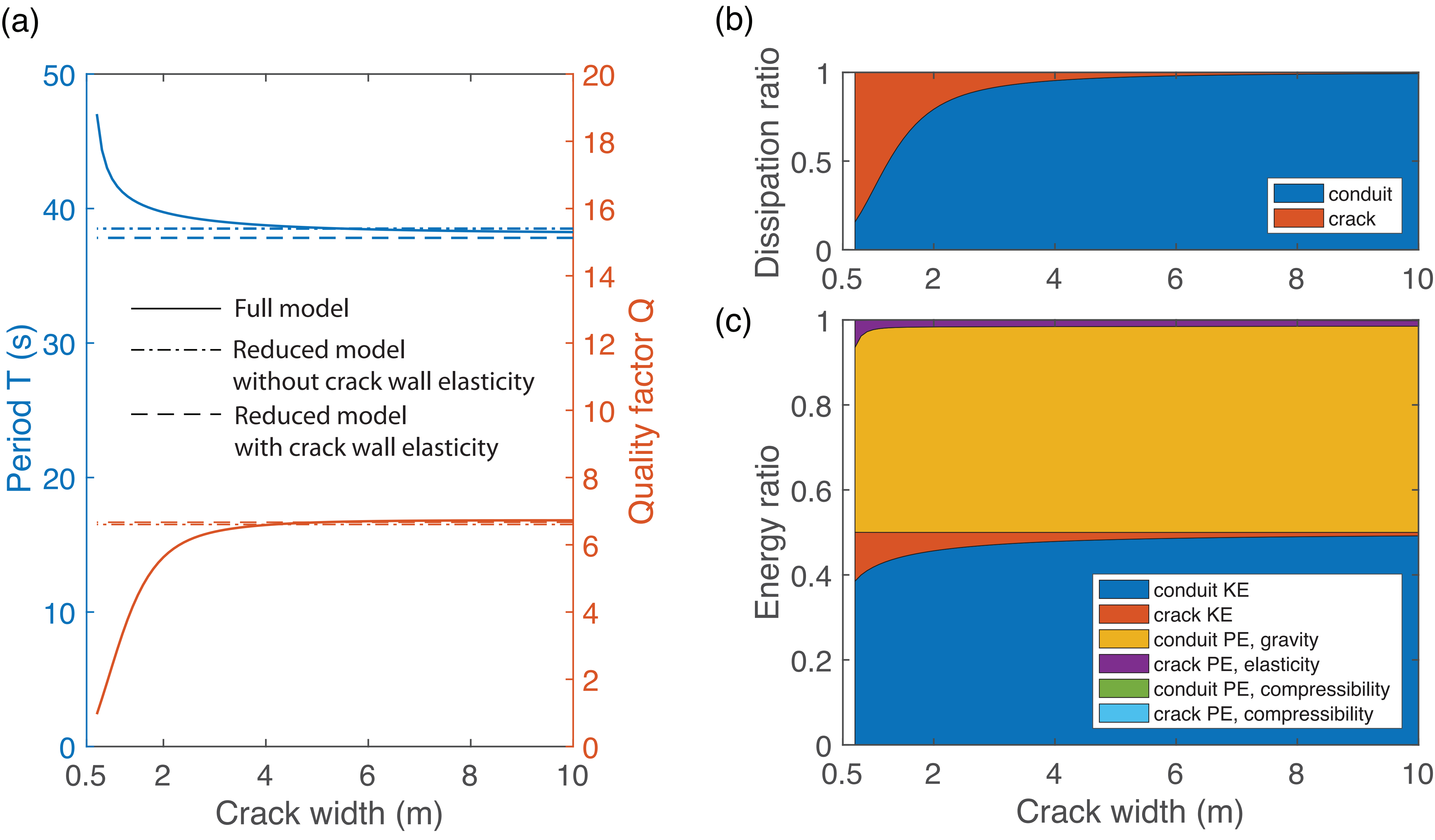
(a)
Period T (s)
Quality factor Q
Crack width (m)
Full model
Reduced model
without crack wall elasticity
Reduced model
with crack wall elasticity
(b)
Dissipation ratio
conduit
crack
(c)
Energy ratio
conduit KE
crack KE
conduit PE, gravity
crack PE, elasticity
conduit PE, compressibility
crack PE, compressibility
Crack width (m)